iScience

CellPress
OPEN ACCESS

Article

Hematologic DNMT3A reduction and high-fat diet synergize to promote weight gain and tissue inflammation

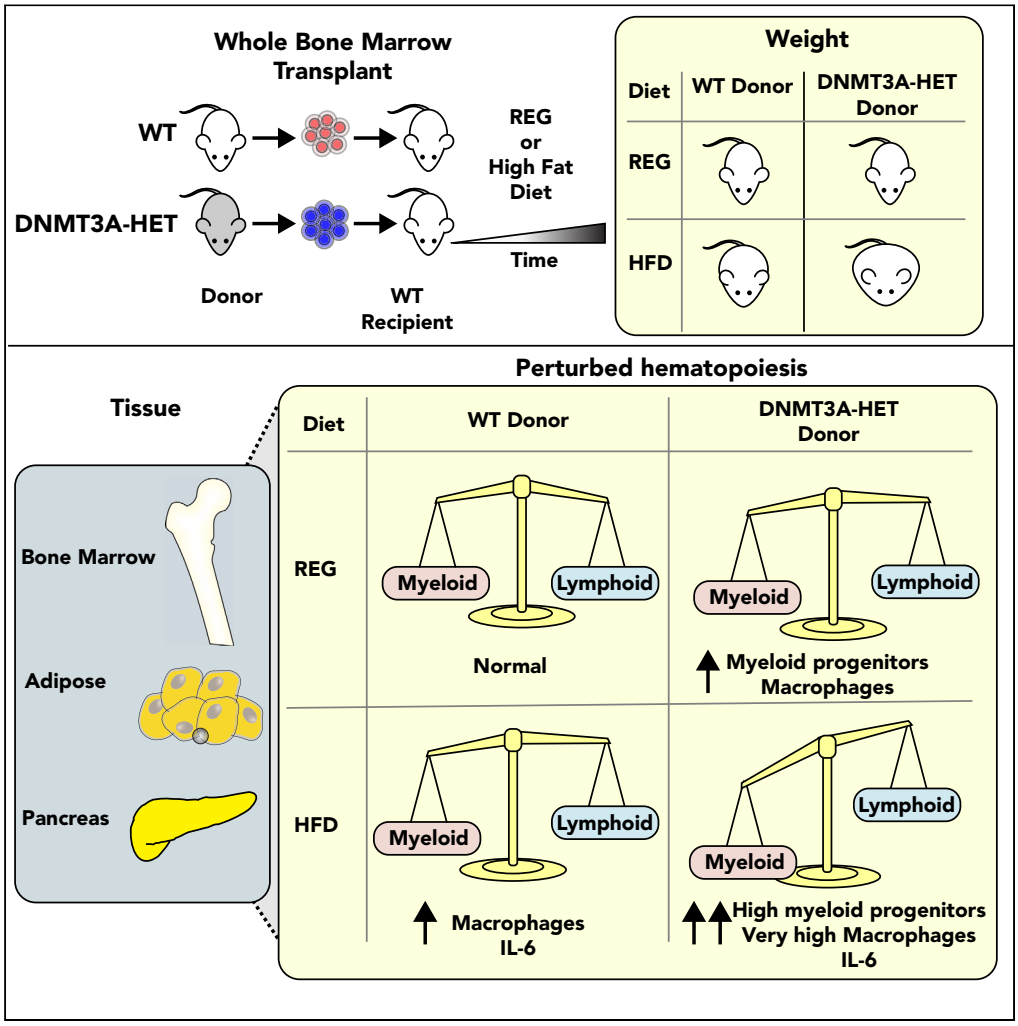

Jaime M. Reyes, Ayala Tovy, Linda Zhang, ..., Ronald J. Parchem, Rachel E. Rau, Margaret A. Goodell

goodell@bcm.edu

Highlights

DNMT3A loss in the blood combined with high-fat diet may accelerate weight gain

High-fat diet increases DNMT3A-mutant macrophages in adipose and pancreas tissue

DNMT3A establishes DNA methylation during macrophage differentiation from HSCs

Loss of DNMT3A leads to activated inflammatory pathways in HSCs and their progeny

Reyes et al., iScience 27, 109122
March 15, 2024
https://doi.org/10.1016/j.isci.2024.109122

iScience

CellPress
OPEN ACCESS

Article

Hematologic DNMT3A reduction and high-fat diet synergize to promote weight gain and tissue inflammation

Jaime M. Reyes,[1,2,3,13] Ayala Tovy,[1,2,13] Linda Zhang,[1,2,4,8] Angelina S. Bortoletto,[1,2,4,8] Carina Rosas,[1,2] Chun-Wei Chen,[1,2,3] Sarah M. Waldvogel,[1,2,5,8] Anna G. Guzman,[1,2] Rogelio Aguilar,[1,6] Sinjini Gupta,[1,2] Ling Liu,[9,11] Matthew T. Buckley,[10] Kalyani R. Patel,[7] Andrea N. Marcogliese,[7] Yumei Li,[3] Choladda V. Curry,[7] Thomas Rando,[9,11,12] Anne Brunet,[10,11] Ronald J. Parchem,[1,2] Rachel E. Rau,[1,6] and Margaret A. Goodell[1,2,3,14,*]

SUMMARY

During aging, blood cell production becomes dominated by a limited number of variant hematopoietic stem cell (HSC) clones. Differentiated progeny of variant HSCs are thought to mediate the detrimental effects of such clonal hematopoiesis on organismal health, but the mechanisms are poorly understood. While somatic mutations in *DNA methyltransferase 3A* (DNMT3A) frequently drive clonal dominance, the aging milieu also likely contributes. Here, we examined in mice the interaction between high-fat diet (HFD) and reduced DNMT3A in hematopoietic cells; strikingly, this combination led to weight gain. HFD amplified pro-inflammatory pathways and upregulated inflammation-associated genes in mutant cells along a pro-myeloid trajectory. Aberrant DNA methylation during myeloid differentiation and in response to HFD led to pro-inflammatory activation and maintenance of stemness genes. These findings suggest that reduced DNMT3A in hematopoietic cells contributes to weight gain, inflammation, and metabolic dysfunction, highlighting a role for DNMT3A loss in the development of metabolic disorders.

INTRODUCTION

Aging in humans is invariably accompanied by the development of clonal hematopoiesis (CH), in which one or a few variant hematopoietic stem cells (HSCs) dominate blood production. CH is associated with an increased risk for hematologic disease and cardiovascular events as well as all-cause mortality.[1–3] The most common driver of CH is somatic mutation of the gene encoding DNA methyltransferase 3A (*DNMT3A*).[4,5] DNMT3A is important for establishing DNA methylation patterns during development, regulating gene expression, and maintaining 3D genome structure.[6–8]

In hematopoietic stem and progenitor cells (HSPCs), the loss of DNMT3A function leads to a bias toward self-renewal at the expense of differentiation.[9–11] The enhanced self-renewal capacity of DNMT3A-mutant stem cells may contribute to the clonal expansion of DNMT3A-mutant cells,[12–14] thereby increasing the risk of developing hematologic malignancies associated with DNMT3A loss.[15–17] However, the broader mechanisms that connect DNMT3A-mutant CH to different pathologies are not yet fully understood. Furthermore, although the inflammatory state driven by environmental factors such as infection, smoking, or diet is thought to be an important factor in the development of CH-associated phenotypes, the precise mechanisms through which DNMT3A-mutant HSPCs are influenced by these cues remain incompletely elucidated.[18]

The methylcytosine dioxygenase TET2 is another gene frequently mutated in CH. Interestingly, several studies have shown that the downstream progeny of mutant TET2 HSPCs, mainly macrophages and monocytes, may mediate the distal tissue effects of mutant TET2-mediated

[1]Stem Cells and Regenerative Medicine Center, Baylor College of Medicine, Houston, TX, USA
[2]Department of Molecular and Cellular Biology, Baylor College of Medicine, Houston, TX, USA
[3]Department of Molecular and Human Genetics, Baylor College of Medicine, Houston, TX, USA
[4]Graduate Program in Translational Biology and Molecular Medicine, Baylor College of Medicine, Houston, TX, USA
[5]Cancer and Cell Biology Graduate Program, Baylor College of Medicine, Houston, TX, USA
[6]Department of Pediatrics, Baylor College of Medicine and Texas Children's Hospital, Houston, TX, USA
[7]Department of Pathology & Immunology, Baylor College of Medicine, Houston, TX, USA
[8]Medical Scientist Training Program, Baylor College of Medicine, Houston, TX, USA
[9]Department of Neurology and Neurological Sciences, Stanford University School of Medicine, Stanford, CA, USA
[10]Department of Genetics, Stanford University, Palo Alto, CA, USA
[11]Paul F. Glenn Center for the Biology of Aging, Stanford University, Palo Alto, CA, USA
[12]Present address: Broad Stem Cell Research Center, University of California, Los Angeles, Los Angeles, CA, USA
[13]These authors contributed equally
[14]Lead contact
*Correspondence: goodell@bcm.edu
https://doi.org/10.1016/j.isci.2024.109122

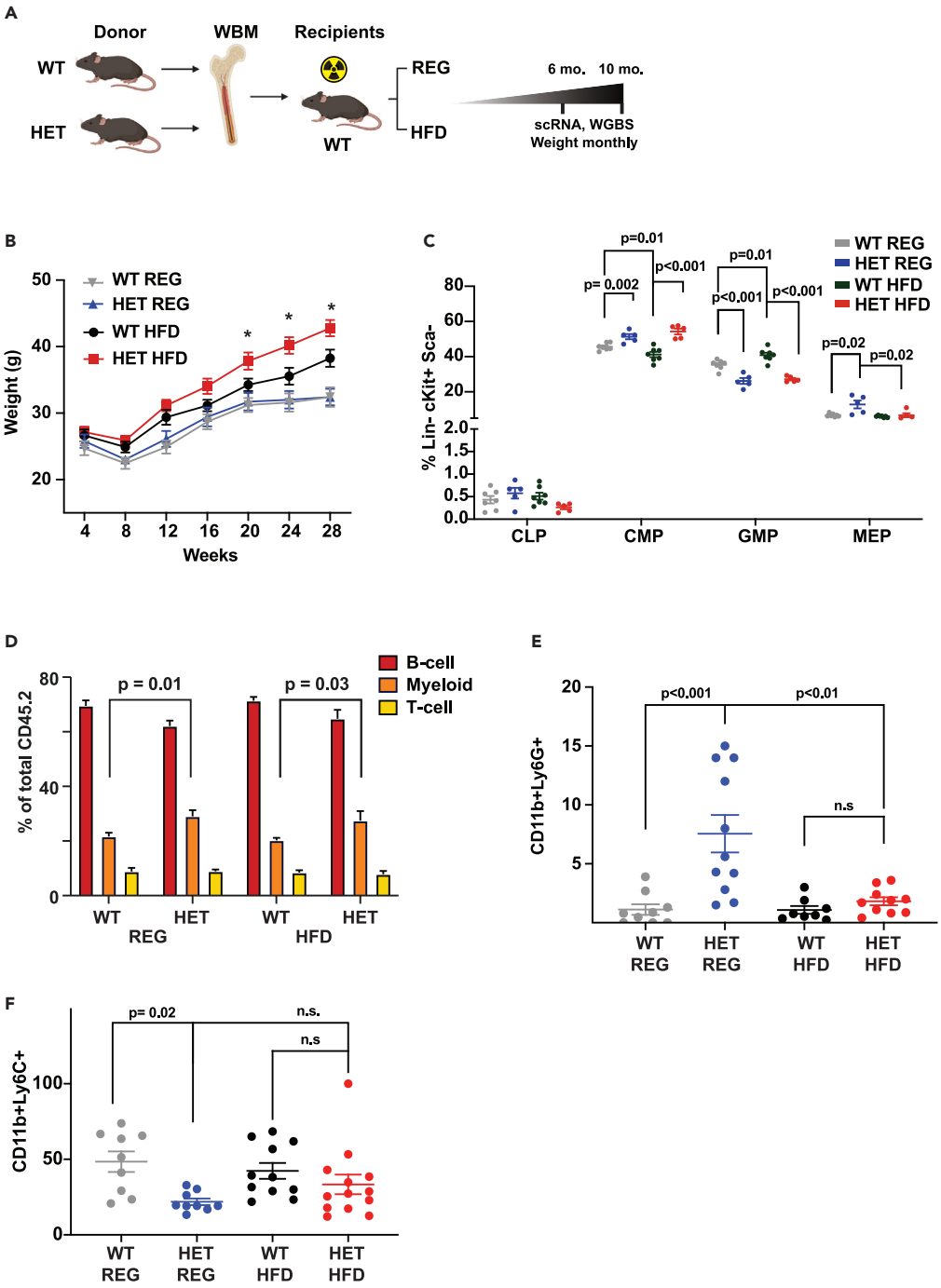

Figure 1. Circulating hematopoietic cells with reduced DNMT3A accelerate weight gain in mice on high-fat diet

(A) Experimental design. Bone marrow from wild-type (WT) or *Dnmt3a*$^{+/-}$ (HET) mice was extracted and infused into irradiated WT recipients. Four weeks after transplantation, recipients were divided into groups and placed on high-fat diet (HFD) or regular diet (REG). Weight was monitored monthly. Donor cells bear the CD45.2 marker on all nucleated blood cells, while recipients bear the CD45.1 marker, allowing donor and recipients to be tracked in all blood and bone marrow lineages.

(B) Weights over time of mice engrafted with WT or *Dnmt3a*-HET bone marrow fed either HFD or regular diet (REG). Two-way ANOVA test was used to determine significance. N = 8–10 male mice per group. (* denotes p value <0.05). Data are represented as mean ± SEM. Experiment repeated twice.

(C) Quantification of flow-cytometric data depicting the percent of bone marrow common lymphoid progenitors (CLPs), common myeloid progenitors (CMPs), granulocyte monocyte progenitors (GMPs), and megakaryocytic erythrocytic progenitors (MEPs) from indicated 6 months post-transplant recipient mice (regular

Figure 1. *Continued*

chow- REG, high-fat diet -HFD). Gating strategy is in Figure S1, and two-way ANOVA test was used to determine significance. Data are represented as mean ± SEM.

(D) Relative proportion of B cells (B), T cells (T), and Myeloid cells (M) as a percentage of total donor cells (CD45.2) measured by flow cytometry 10 months after transplantation. Lineages defined as B220+ (B), $CD4^+$ and $CD8^+$ (T) and CD11b+ (M). Data are represented as mean ± SEM.

(E) Quantification of flow-cytometric data depicting the percent of donor-derived Ly6g+ neutrophils as a proportion of total CD11b+ myeloid cells in peripheral blood 10 months post-transplant. Statistical significance was determined using a one-way ANOVA. Data are represented as mean ± SEM.

(F) Quantification of flow-cytometric data depicting the percent of donor-derived Ly6C+ monocytes as a proportion of total CD11b+ myeloid cells in peripheral blood 10 months post-transplant. Statistical significance was determined using a one-way ANOVA. Data are represented as mean ± SEM.

CH.[19] In a mouse model of *TET2*-driven CH, mutant macrophages overexpressing the inflammatory cytokine interleukin 6 (IL-6) accelerated cardiovascular disease.[20] Similarly, patients with heart failure and *DNMT3A*-mutant CH exhibited increased transcription of IL-6 and tumor necrosis factor alpha (TNF-α) in myeloid cells.[21] However, while these and other studies have suggested that CH, at least in the context of certain mutations, leads to hyperinflammatory immune cells, whether the observed changes were inherent to the variant HSPC clone or pervasive across peripheral blood was not clear.

Among the most common sources of inflammation in Western countries is a high-fat diet (HFD). Highly correlated with obesity, HFD promotes inflammatory signaling and has been shown to impact HSC function, skewing differentiation toward the myeloid lineage,[22] a known feature of CH.

Here, we aimed to investigate the relationship between an HFD and reduced DNMT3A levels in terms of their effects on myeloid differentiation and impact on distal tissues. We observed that the combination of mutant cells in the blood and HFD exposure led to weight gain and insulin resistance. Notably, there was a disproportionate accumulation of mutant macrophages in distal tissues compared to their presence in the blood. This finding suggested that the macrophages with reduced DNMT3A exhibited an increased propensity to infiltrate peripheral tissues. Furthermore, our analysis revealed that macrophages lacking DNMT3A displayed heightened immune response characteristics attributed to loss of DNA methylation. Taken together, our findings provide insights into the mechanistic link between the loss of DNMT3A and myeloid cell behavior and shed light on the potential role of DNMT3A in modulating inflammatory responses and its impact on the pathogenesis of metabolic disorders associated with HFD.

RESULTS

Reduced hematopoietic DNMT3A accelerates weight gain in mice on an HFD

To examine the interplay between HFD and CH, we modeled CH by transplanting bone marrow cells from mice lacking one copy of *Dnmt3a* ($Dnmt3a^{+/-}$, heterozygous, referred to here as HET) or from wild-type (WT) mice into male recipients (Figure 1A). After engraftment was confirmed 4 weeks later, mice were divided into 4 groups and fed either regular chow (REG) or HFD (45% kcal fat) (Figure 1A). Starting 20 weeks after transplantation, we noticed that mice on HFD and engrafted with HET cells had a greater increase in weight than their counterparts engrafted with WT cells (Figure 1B). By 10 months post-transplant, the weight of recipients of HET bone marrow fed with HFD was 2.71 standard deviations (SDs) above the mean of recipients with WT cells (Figure S1A). This finding suggests a direct impact of the *Dnmt3a* hematopoietic cells on weight regulation. Notably, the same experiment using female recipients did not result in statistically significant weight gain suggesting sex-specific effects (Figure S1B).

HFD alters HSPC cell composition differentially in WT compared to HET progenitors

The common pathology of HFD is low-grade inflammation that results in activation of inflammatory cascades and a shift in abundance of pro-inflammatory immune cells specifically of the myeloid lineage.[22]To examine if HFD and reduced DNMT3A impacted immune cell reconstitution, we analyzed the proportions of bone marrow progenitors and differentiated cells derived from WT- and HET-transplanted mice (Figure 1C). Although, we did not observe major differences in the HSC compartment, HFD did impact myeloid-associated but not lymphoid progenitors in both WT and HET mice (Figures S1C; Figure 1C). WT mice had decreased common myeloid progenitors (CMPs) and increased granulocyte monocyte progenitors (GMPs) with HFD. In contrast, HET mice showed expansion of CMP and megakaryocytic erythrocytic progenitors (MEP) relative to WT-transplanted mice, but this was regardless of diet. This expansion of HET myeloid progenitors was accompanied by more mature myeloid cells in the blood regardless of diet (Figure 1D). Of the myeloid cells, HET-transplanted mice displayed an increase in neutrophils (CD11b+, Ly6G+) at the expense of monocytes (Ly6C+ cells) compared to WT controls (Figures 1E and 1F). Although the mechanism for neutrophil expansion is unclear, it is consistent with our previous observations in HET mice and in patients with germline loss of *DNMT3A*.[11]

Complete blood counts (CBC) on peripheral blood from recipient mice revealed similar trends. HET bone marrow recipients had increased total white blood cells regardless of diet (Figures S1D and S1E). HET-transplanted mice fed HFD had a significantly increased mean corpuscular volume (MCV), mean corpuscular hemoglobin (MCH), and decreased platelet numbers (Figure S1D). Overall, these findings indicate that, while the proportion of progenitors in WT-transplanted mice changed in context of the HFD, cells lacking DNMT3A did not respond similarly. Therefore, the acceleration of weight gain in the context of HET bone marrow and HFD occurs through a mechanism other than peripheral blood immune cell composition.

Table 1. Hematological findings in transplanted mice

Mouse ID	Transplant	Donor	Diet	Splenic phenotype	Adipose phenotype	Notes
#57	WBM	WT	HFD	Reactive lymphoid and plasmacytic hyperplasia	Few small lymphoid aggregates. One with plasma cells, otherwise looks normal	NA
#40	WBM	HET	REG	Normal	Focal mild infiltrate of scattered mast cells. Also, small focus of chronic inflammation	NA
#44	WBM	HET	REG	Reactive lymphoid and plasmacytic hyperplasia	Small focus of chronic inflammation, otherwise looks normal	NA
#26	WBM	HET	HFD	Reactive lymphoid hyperplasia	Scattered focal chronic inflammation	In bone section increased focal hemosiderin deposition
#32	WBM	HET	HFD	Leukemia with markedly expanded red pulp. White pulp nearly absent.	Scattered focal chronic inflammation	Tumor attached to liver with foci of prominent microvesicular and macrovesicular steatosis mild portal and lobular chronic inflammation

HFD contributes to chronic inflammation and leukemogenesis in *Dnmt3a*-HET-transplanted mice

To further characterize the impact of HET bone marrow in combination with HFD on disease outcomes, we performed pathological analysis on mice 10 months post-transplant. We evaluated hematopoietic organs (bone, spleen) and non-hematopoietic organs (adipose and tumors, if detected) (3 cohorts, 10–12 mice per condition). In addition, we monitored one cohort of mice for an additional 12 months to determine effects on overall survival. Ten months after transplantation, we observed larger spleens and increased tissue inflammation including formation of lymphoid and myeloid immune cell aggregates in spleen and adipose tissue sections from HET-transplanted mice; these phenotypes were exacerbated by HFD (Table 1; Figures S2A–S2C). Starting at 12 months post-transplant, several HET-transplanted mice, mainly on HFD, became moribund, exhibiting lethargy, ruffled fur, and weight loss (Figure S2E). In the affected mice, we found increased myeloid infiltrates and leukemia development (Figure S2C). HET-transplanted mice fed an HFD exhibited shorter lifespan suggesting the combination of circulating *Dnmt3a*-HET cells and HFD has detrimental effects on health and survival (Figure S2D).

Mice with *Dnmt3a*-HET bone marrow develop glucose intolerance

To identify mechanisms by which reduction of DNMT3A in bone marrow impacts weight gain, we investigated tissue function in transplanted mice. Adipose tissue is among the key organs impacted by HFD.[23] Adipose tissue expands with lipid storage, leading to oxidative stress and inflammation. Moreover, remodeling of adipose tissue and the secretion of adipose cytokines and chemokines lead to recruitment of myeloid cells.[24] In turn, myeloid cells, particularly macrophages, can further infiltrate the adipose tissue to secrete additional inflammatory cytokines.

As HET-transplanted mice showed increased mature myeloid cells as well as myeloid progenitors, we examined whether this myeloid expansion was accompanied by higher infiltration of macrophages into adipose tissue. While we did not observe a significant difference in the total number of immune cells present in adipose tissue 10 months post-transplantation, we found a significantly higher number of macrophages (~1.5-fold) in recipients transplanted with HET cells on HFD, with a similar trend on REG although not statistically significant (Figure 2A). At this time point, HFD-HET-transplanted mice already show weight change which could impact macrophage distribution; therefore, we also examined macrophage infiltration at an earlier time point. Notably, at 6 months post-transplant, we only observed an increase in HET macrophages following HFD, suggesting that HFD amplifies macrophage infiltration which takes longer under REG conditions. Immunohistochemistry analysis of macrophages (F4/80+) surrounding adipocytes, also known as crown structures, showed that HET-transplanted mice on an HFD displayed the greatest increase in adipose tissue macrophages. F4/80+ cells constituted 3.02% of the area imaged in HET-HFD mice compared to WT on HFD at 1.09% (Figures 2B and S3D). Notably, WT recipients on HFD had similar levels of adipose tissue macrophages as HET recipients on a regular diet (Figures 2A, 2B, S3A, and S3D).

Next, we asked if increased macrophage infiltration in HET-transplanted mice was also detectable in peripheral tissues other than adipose. We quantified macrophage infiltration into liver, spleen, and pancreas by flow cytometry. We found a significant increase in HET-derived macrophages in the pancreas, liver, and spleen of mice fed HFD (Figures 2C; Figures S3A and S3B). In the bone marrow however, HFD increased macrophages in both WT- and HET-transplanted mice (Figure S3C). These data suggest that the HFD was sufficient to lead to increased macrophage infiltration to some tissues (e.g., spleen and pancreas), and this is exacerbated in the context of reduced DNMT3A.

In human obesity the overall increase in macrophages infiltrating into adipose and pancreas leads to tissue dysfunction and the development of metabolic disease affecting glucose and insulin metabolism.[25] To test whether HFD combined with reduced DNMT3A impacts glucose metabolism, we performed a glucose tolerance assay in transplanted mice fed either REG or HFD. At 10 months post-transplant, we observed mild glucose intolerance in the HET-transplanted compared to WT-transplanted mice on regular diet (Figure S3G), and this

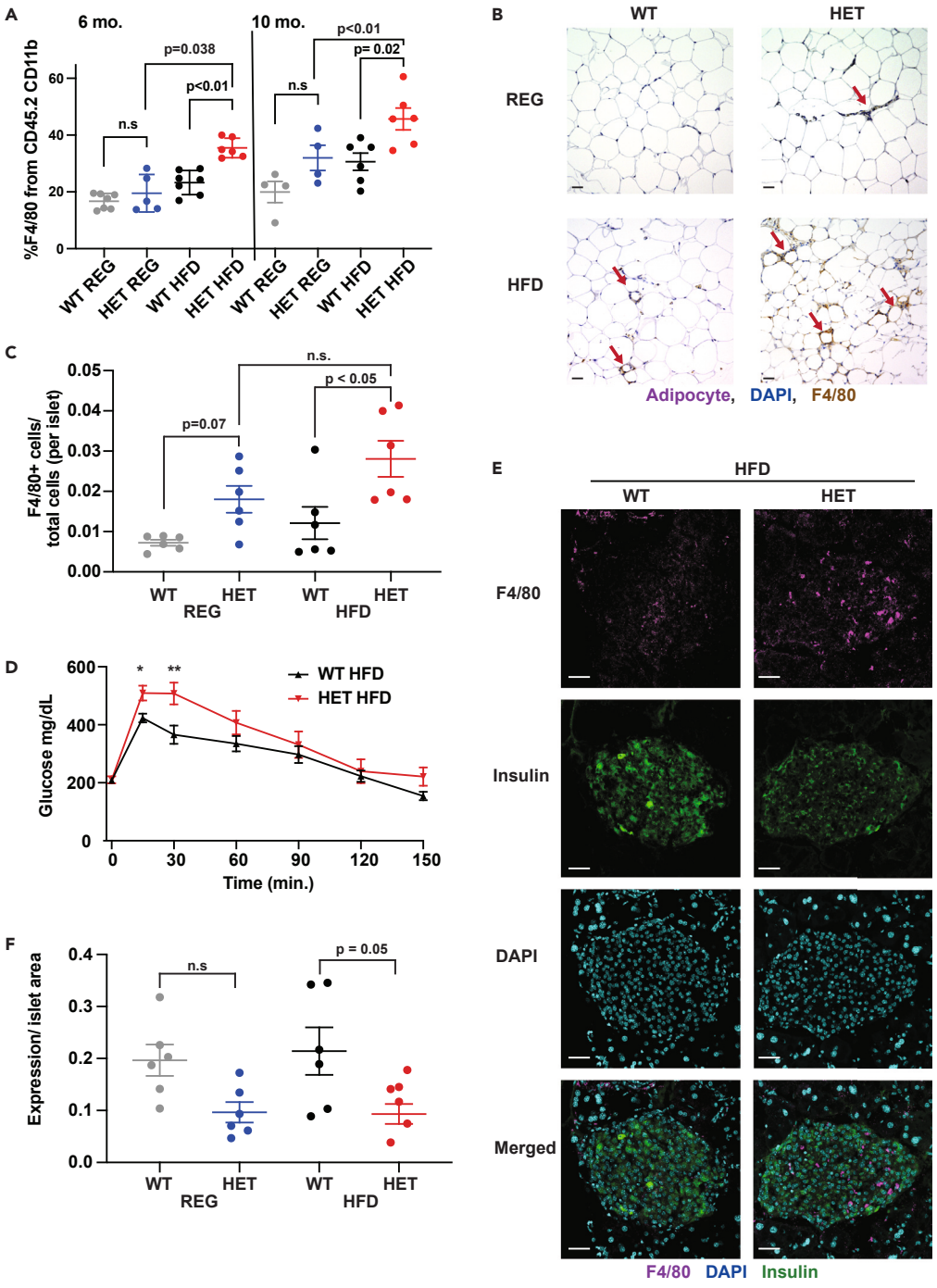

Figure 2. High-fat diet coupled with circulating *Dnmt3a+/−* cells impacts glucose metabolism

(A) Quantification of macrophages (F4/80+, CD11b+) as a percentage of donor-derived (CD45.2) myeloid cells (CD11b+) extracted from subcutaneous adipose of receipt mice in REG or HFD at 6 months compared to 10 months post-transplant. Tissue was processed to isolate stromal vascular cells which were then subjected to flow-cytometric analyses with the denoted markers. Statistical significance was determined using two-way ANOVA. Data are represented as mean ± SEM.

(B) Microscopic imaging of subcutaneous adipose depots collected 40 months after transplantation (as in Figure 1A). Tissues were collected in 4% formalin, embedded in paraffin, and stained with hematoxylin and eosin (H&E), DAPI, and antibody against F4/80 to detect adipocytes, all nuclei (blue), and F4/80 macrophages (brown), respectively. Arrows denote inflammatory crown structures surrounding adipocytes. Image is taken at 20× magnification. Scale bars (bottom left) indicate 100 μm.

Figure 2. *Continued*

(C) Quantification of F4/80 macrophages as a fraction of total cells per islet. Two islets were quantified for each of three mice for each group using the Analyze Particles function of ImageJ (See STAR Methods for details). Significance testing was performed using one-way ANOVA. Data are represented as mean ± SEM.

(D) Glucose tolerance test 10 months after transplantation in mice fed HFD. Mice were fasted for 12 h prior to testing, infused with glucose intravenously at time zero, and measured for glucose in the peripheral blood in 30-min intervals. N = 10–12 per group. Significance testing was performed using one-way ANOVA. Data points are presented as mean ± SE. * pval <0.05, ** pval <0.01.

(E) Representative pancreatic beta islets from recipient mice (as in Figure 1A) fed an HFD. Pancreases were removed 10 months after transplantation, frozen sectioned, and immunostained for F4/80 macrophages (purple), Insulin (green), or all nuclei (DAPI, blue). Scale bars (bottom left) indicate 100 μm.

(F) Quantification of insulin intensity per islet area. Two islets were quantified for each of three mice for each condition. Insulin expression was determined by analyzing the total insulin signal area per islet area using the Measure and Histogram functions of ImageJ. Significance testing was performed using ANOVA. Data are represented as mean ± SEM.

difference was more significant in mice on HFD (Figure 2D). HET-transplanted mice on HFD had impaired glucose uptake and needed more time to clear glucose from peripheral blood than WT mice on HFD.

Compromised glucose uptake due to diet-induced inflammation and weight gain can correlate with dysfunction of pancreatic insulin-secreting islet cells. Eventually the damage to those cells may reduce insulin-secreting cells leading to insulin resistance.[26] To determine the impact of HFD on islets, we stained sections of pancreatic tissue from mice from each condition and used immunofluorescence to quantify islets, macrophages, and total insulin. Although the total number of islets did not differ among groups (Figure S3F), HET mice had significantly reduced insulin expression (Figures 2E and 2F). While decreased release of insulin correlated with an increase in F4/80 macrophages in islets, including a significant increase in F4/80 macrophages in HET HFD (Figure 2C), these changes did not affect insulin tolerance in the periphery (Figure S3H). Together with glucose tolerance and histology quantification, our data indicate that *Dnmt3a*-HET bone marrow impacts glucose regulation and increases susceptibility to insulin resistance, especially in the context of HFD.

Dnmt3a-HET shows myeloid lineage skewing regardless of diet

Thus far, our results suggest that the presence of DNMT3A mutant myeloid cells, specifically macrophages, can impact organismal metabolism and that HFD magnifies this phenomenon. We next sought to examine how partial loss of *Dnmt3a* impacts stem and progenitor cell transcriptional programs in response to HFD. We performed single-cell RNA sequencing (scRNA-seq) on HSPCs (defined as Lin-, Sca1+, cKit+, termed LSK) derived from mice 10-month post-transplant. We integrated and normalized libraries from 41,266 cells (2 mice per group) sequenced to an average depth of 54,609 reads per cell and performed quality control analyses using Seurat pipelines (Figure 3A; Figures S4A and S4B). In WT mice, we found that HFD increased the proportion of cells in a quiescent (G1) state at the expense of proliferating cells (G2/M and S phase) (Figure S4D). In contrast, diet did not significantly change the proportion of *Dnmt3a*-HET cells in each phase of the cell cycle, suggesting that differences in cellular function are not due to the proliferation state but may arise from differential transcription.

To analyze changes within our progenitor (LSK) dataset, we next performed cell type annotation and assigned each cell to a cluster by combining SingleR[27] with manually curated known HSPC marker genes (*Slamf1*, *Cd48*, *Flt3*, Figure S4E) (See Figure S4E and STAR Methods for details). We identified six major cell populations within the progenitors: the HSC compartment, which includes both long and short-term HSCs (LT-HSCs); lympho-myeloid multipotent progenitors (LMPPs); common lymphoid progenitors (CLPs); myeloid progenitors (MyMPPs); mast cell progenitors (Mast); and megakaryocyte-erythroid progenitors (MEPs) (marker genes in STAR Methods). To determine the impact of diet on cell type abundance within progenitors, we calculated the proportion of each cell type in WT- or HET-transplanted mice fed REG or HFD (Figure 3B). We found that HFD increased the proportion of WT HSCs at the expense of lineage-biased progenitors like LMPP and CLP. On the other hand, even on a regular diet, *Dnmt3a*-HET cells maintained a high proportion of HSCs and LMPPs compared to WT mice fed REG. We found that HFD did not significantly redistribute progenitor cell types for *Dnmt3a*-HET cells. Like our analysis of lineage distribution from the flow cytometry analysis, these results indicate that HET cells are skewed toward the myeloid lineage at baseline and that the addition of HFD does not significantly impact their lineage distribution within the stem and progenitor (LSK) compartment.

HFD amplifies expression of pro-inflammatory pathways in *Dnmt3a*-HET cells

Next, we sought to dissect the transcriptional changes occurring in *Dnmt3a*-HET or WT LSK cells under HFD. LSKs encompass defined progenitors as well as those in intermediate or transitional states; this mix of closely related cells may confound differential gene expression analysis performed on a cluster-by-cluster basis. Accordingly, to eliminate possible noise introduced by transitional cells within a cluster, we applied pseudotime inference techniques to assign cells to a cellular differentiation trajectory. Pseudotime methods reorder cells along an approximation of hematopoietic differentiation going from HSCs to mature progenitors like myMPPs, CLPs, or MEPs (Figure 3C; Figure S4F). Within our dataset, we identified four trajectories originating from the stem cell cluster: pro-lymphoid, MEP, mast cell, and pro-myeloid (Figure S4G). After assigning cells to trajectories, we were able to isolate lineages and perform differential gene expression throughout differentiation states.

To dissect transcriptional changes within the pro-myeloid trajectory, we performed differential gene expression and grouped cells by diet and genotype. We first isolated cells along the pro-myeloid trajectory under regular diet and compared HET versus WT cells. We identified several genes, such as that encoding *Tnf-α*, that were significantly upregulated in REG HET cells early on in pseudotime and remained upregulated along the trajectory (Figure 3D). When we compared HFD cells, *Tnf-α* itself was upregulated by diet but was not differentially expressed between WT and HET cells and followed a similar pattern of expression in both genotypes. In addition to genes that were

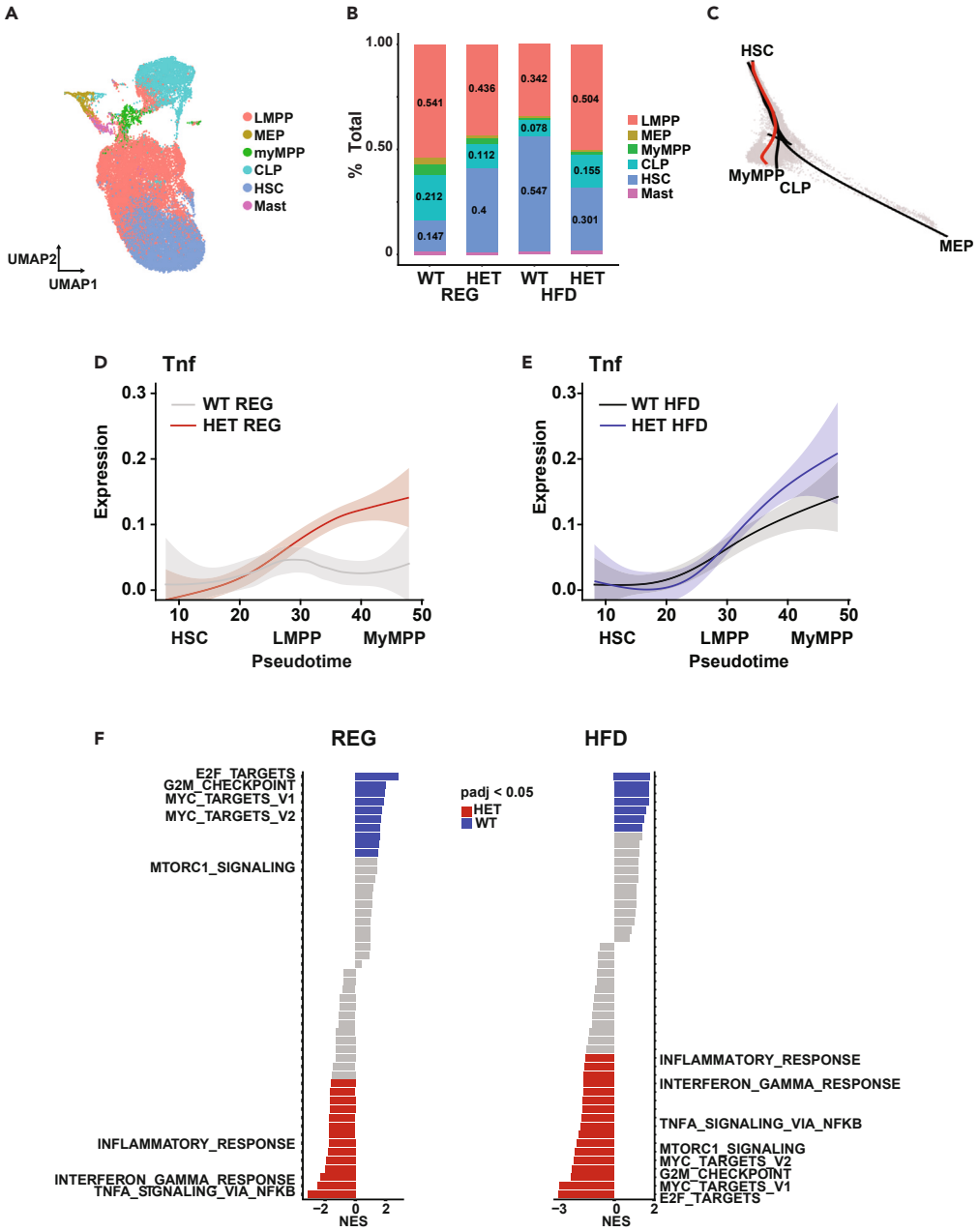

Figure 3. Pro-myeloid stem and progenitor cells from *Dnmt3a*-HET under HFD are transcriptionally enriched for pro-inflammatory pathways

(A) Uniform manifold approximation and projection (UMAP) of hematopoietic progenitors (Lineage^{neg} Sca1+ cKit+, "LSK" cells) (n = 28,984) from mice 10-month after transplantation mice (n = 2 each from separate transplant experiment). Colors indicate annotated cell type. Cell types were annotated using a mapped reference (See STAR Methods) dataset and SingleR. HSC, hematopoietic stem cell; LMPP, lympho-myeloid multipotent progenitor; MyMPP, myeloid multipotent progenitor; CLP, common lymphoid progenitor; MEP, megakaryocyte-erythroid progenitor; Mast, mast cell.

(B) Cell type fractions (as defined in (a)) per condition. Values indicate percent of total cells per condition.

(C) Force-directed graph layout of cell clusters within LSK overlaid with lineage trajectories (solid lines). Red indicates the pro-myeloid trajectory.

(D) Tnf-α gene expression plot for WT or HET cells under REG along the pro-myeloid trajectory. The smoothed line indicates average gene expression along the pseudotime ordered trajectory. Shaded area indicates standard error (SE) for either WT REG (gray) or HET REG (red).

(E) Tnf-α gene expression plot for WT or HET cells under HFD along the pro-myeloid trajectory. Average expression indicated for WT HFD (black) or HET HFD (blue).

(F) Gene set enrichment analysis for genes differentially expressed between HET and WT cells within the pro-myeloid trajectory under REG (left) or HFD (right). Bars indicate changes in pathway ranks between diets with those in red and blue indicating significantly enriched pathways in HET or WT, respectively. Significance determined using Benjamin-Hochberg adjusted p value. p value <0.05.

upregulated within later stages of differentiation, we identified genes that were differentially expressed within early stem-like states. *Socs3*, for example (Figures S4H and S4I), was not expressed in WT cells from mice fed REG but was upregulated in HET stem-like cells. Under HFD, *Socs3* was upregulated by both WT cells and HET. These observations indicate that HET cells, regardless of diet, retain high expression of genes that are normally induced by HFD in WT cells and may lead to aberrant expression of gene pathways throughout myeloid differentiation.

To further characterize the impact of HFD and reduced DNMT3A, particularly within the myeloid lineage, we analyzed pathways differentially expressed along the pro-myeloid lineage trajectory. As the variant cells within the myeloid lineage confer the phenotypes observed in our transplanted mice, we performed gene set enrichment analysis among our four conditions. On regular diet, WT cells were enriched for cell-cycle-associated pathways (E2F targets, G2M checkpoint, MYC targets, Figure 3F) while HET cells were enriched for TNF-α signaling and other pro-inflammatory pathways. In HFD, these same pathways were more strongly enriched in HET cells, with the addition of many cell-cycle-related pathways. Regardless of diet, we found that HET cells were enriched for pro-inflammatory pathways (TNF-α signaling via nuclear factor κB [NF-κB], inflammatory response, interferon (IFN) gamma signaling, Figure 3F). These findings indicate that HET cells exhibit at baseline the transcriptional changes HFD causes in WT cells, and that diet seems to amplify inflammatory gene expression in HET stem and progenitor cells.

Our analyses showed that HFD led to an increase in HET donor macrophage infiltration into adipose tissue and a heightened inflammatory state. We considered whether immune cells in adipose tissue of non-transplanted germline HET mice would exhibit similar alterations, particularly given that adipose tissue of HET mice itself shows increased inflammatory signaling.[28] We performed scRNA-seq on sorted $CD45^+$ cells from adipose tissue of germline HET and WT mice. We grouped SingleR-annotated immune cells based on their hematopoietic lineage into myeloid, lymphoid, mast cells, and neutrophil clusters (Figure 4A). We performed transcriptomic pathway analysis and found that overall HET cells showed differential regulation of inflammatory-related pathways (Figure S5B). We then specifically analyzed expression of pro-inflammatory IL-6 in the myeloid cluster ($CD45^+$CD11b +) and observed higher IL-6 expression in HET cells compared to WT (Figure 4B). These results support our observations that HET immune cells are primed for higher activation of pro-inflammatory genes such as IL-6 that can then impact tissue function even in absence of HFD.

HFD typically leads to elevated levels of circulating IL-6.[29] To better understand the overall impact of IL-6 in REG and HFD following WT and HET transplant, we analyzed IL-6 levels in multiple tissues: in circulation (plasma), in bone marrow stem and progenitor cells (cKit+ cells), and in $CD45^+$ cells isolated from adipose tissue of recipients of either WT or HET cells on HFD. We could not perform similar analysis on REG due to lower cell counts (Figures 4C and 4D). Our results demonstrate a ~2-fold increase in circulating plasma IL-6 and cellular IL-6 particularly in mice that received HET donors and were fed HFD. Also, these results suggest that loss of *Dnmt3a* in combination with HFD induces upregulation of IL-6 transcription and production, which is reflected both intrinsically within HET cells and systemically in circulation.

IL-6 increases transcription of pro-inflammatory pathways in *Dnmt3a*-HET adipose tissue

To further delineate the interplay between IL-6 and DNMT3A-derived myeloid cells, we conducted *in vitro* differentiation of bone marrow cells into macrophages with and without IL-6 supplementation (Figure 5A). We focused our investigation on macrophages given that they were significantly more abundant in HFD-HET-recipient mice. Strikingly, HET-derived *in vitro*-differentiated macrophages intrinsically displayed 2-fold more IL-6 protein expression on day 7 of differentiation compared to WT cells (Figure 5B), aligned with our scRNA-seq data from mice. Notably, partial loss of DNMT3A did not impact macrophage differentiation rate or phagocytic activity, with or without IL-6 (Figure S6A; Figures 5C and 5E). These findings suggest a potential involvement of DNMT3A in modulating IL-6 expression during myeloid differentiation without necessarily impacting their phagocytic function.

To investigate the impact of circulating IL-6 as occurs in HFD on WT and HET cells gene expression, we added IL-6 on day 7 of differentiation for an additional 2 days and performed RNA-seq analyses on IL-6-treated and untreated macrophages. First, by using principal-component analysis (PCA), we observed separation of HET and WT samples in both untreated (control) and IL-6-treated samples (Figure S6B). We performed unsupervised hierarchical analysis on normalized transcripts to identify global changes in gene expression across conditions (Figure 5D). Notably, we identified subsets of genes that clustered by IL-6 treatment (Groups I and III) or by *Dnmt3a* heterozygosity (Groups II and V). Pathway enrichment analysis using the Molecular Signatures Database (MSigDB) was used to compute gene overlaps against the hallmarks collection of pathways. As expected, IL-6 treatment enriched for IL-6 signaling (Figures S6C–S6E). In the HET_NT group (Group II), we observed significant overlap with TNF-α signaling. Interestingly, Group V (upregulated in HET_NT and HET_IL-6) had strong overlap with pro-inflammatory pathways, suggesting that IL-6 stimulation may amplify genes already expressed in untreated HET macrophages (Figure S6E). To quantify the specific transcriptional differences between HET and WT macrophages upon IL-6 treatment, we performed differential gene expression analysis on IL-6-treated HET- and WT-derived macrophages (Figure 5F). HET cells upregulated pro-inflammatory pathways and genes (Figure 5G). Taken together, loss of DNMT3A leads to transcriptional changes at pro-inflammatory genes and, when treated with IL-6, these pathways are further impacted.

We then puzzled whether genes differentially expressed in *in vitro*-derived macrophages were similarly expressed *in vivo*. We therefore used genes upregulated in the *in vitro* HET-derived macrophages to perform gene set enrichment analysis using the *in vivo* scRNA dataset of adipose tissue immune cells (Figure 5B), comparing HET versus WT cells. In lymphoid cells, genes upregulated in HET macrophages were not enriched in either HET or WT cells. HET myeloid cells, however, showed strong enrichment for macrophage genes, corroborating evidence that HET cells, derived either *in vitro* or *in vivo*, have intrinsic pro-inflammatory transcriptional biases that are specifically enriched in myeloid cells (Figure S6F).

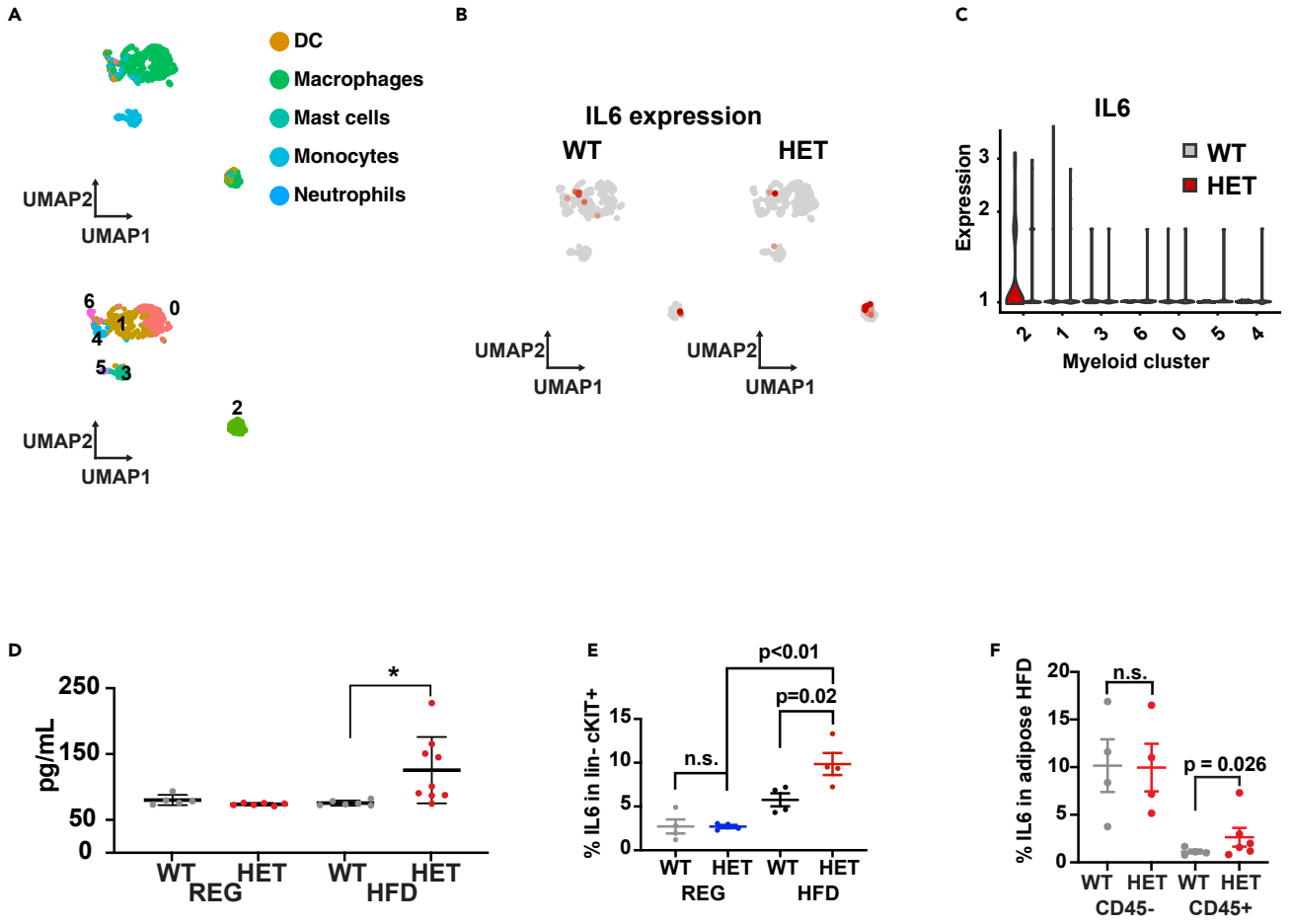

Figure 4. IL-6 is differentially upregulated in recipient mice with HET bone marrow

(A) Uniform manifold approximation and projection (UMAP) of myeloid-derived hematopoietic cells (CD45$^+$, CD11b+ cells) (n = 724) isolated from adipose tissue of 12-months-old WT and germline Dnmt3a-HET mice. Colors indicate annotated cell type. Cell types were annotated using SingleR according ImmGen reference (Top). Clusters were then identified using Seruat function find neighbors (bottom).

(B) Quantification of IL-6 expression in WT and HET in UMAP representation.

(C) Quantification of IL-6 expression across myeloid cell clusters as defined in (A).

(D) Enzyme-linked immunosorbent assay (ELISA) for IL-6 in plasma derived from mice 10 months post-transplant (as in Figure 1A) of WT or HET bone marrow and fed REG or HFD. Significance was determined using one-way ANOVA. Data are represented as mean ± SEM.

(E) Flow-cytometric quantification of IL-6 using fluorescent antibody crosslinking from cKIT+ hematopoietic stem and progenitor cells. Cells were enriched using magnetic column and then assessed for IL-6 fluorescence. Significance was determined using one-way ANOVA. Data are represented as mean ± SEM.

(F) Flow-cytometric quantification of IL-6 using fluorescent antibody crosslinking from adipose tissues derived from transplanted mice fed HFD. Tissue was processed to isolate stromal vascular cells and subject to flow-cytometric analysis with the denoted markers. Cells were gated by Cd45 positivity and assessed for IL-6 fluorescence. Significance was determined using one-way ANOVA. Data are represented as mean ± SEM.

DNMT3A is required for setting the DNA methylation in pluripotency and inflammatory genes during differentiation and following HFD

In the hematopoietic system, loss of DNMT3A is associated with reduced DNA methylation (hypomethylation) near genes involved in maintaining stem cell identity, increased expression of stem cell genes across cell types, and impaired differentiation.[9] How loss of DNMT3A in HSCs leads to functional consequences in downstream progeny remains largely unexplored. Our data indicated that loss of Dnmt3a impacted CMPs and macrophage infiltration and suggested that the HFD magnified HET phenotypes that were also often mildly detected in HET cells on an REG diet, as well as WT cells on HFD.

Here, we sought to investigate whether alterations in DNA methylation due to reduced DNMT3A could account for inflammatory macrophage infiltration and tissue damage. Thus, we examined DNA methylation differences using whole-genome bisulfite sequencing on CMPs and macrophages from WT- and HET-transplanted mice fed either REG or HFD for 6 months post-transplant.

First, we calculated overall DNA methylation levels and defined hypomethylated regions (HMRs) for all conditions (Figure 5A-scheme). Next, we defined how DNA methylation was impacted by HFD in CMPs and in macrophages (MACs), comparing WT to HET. We defined

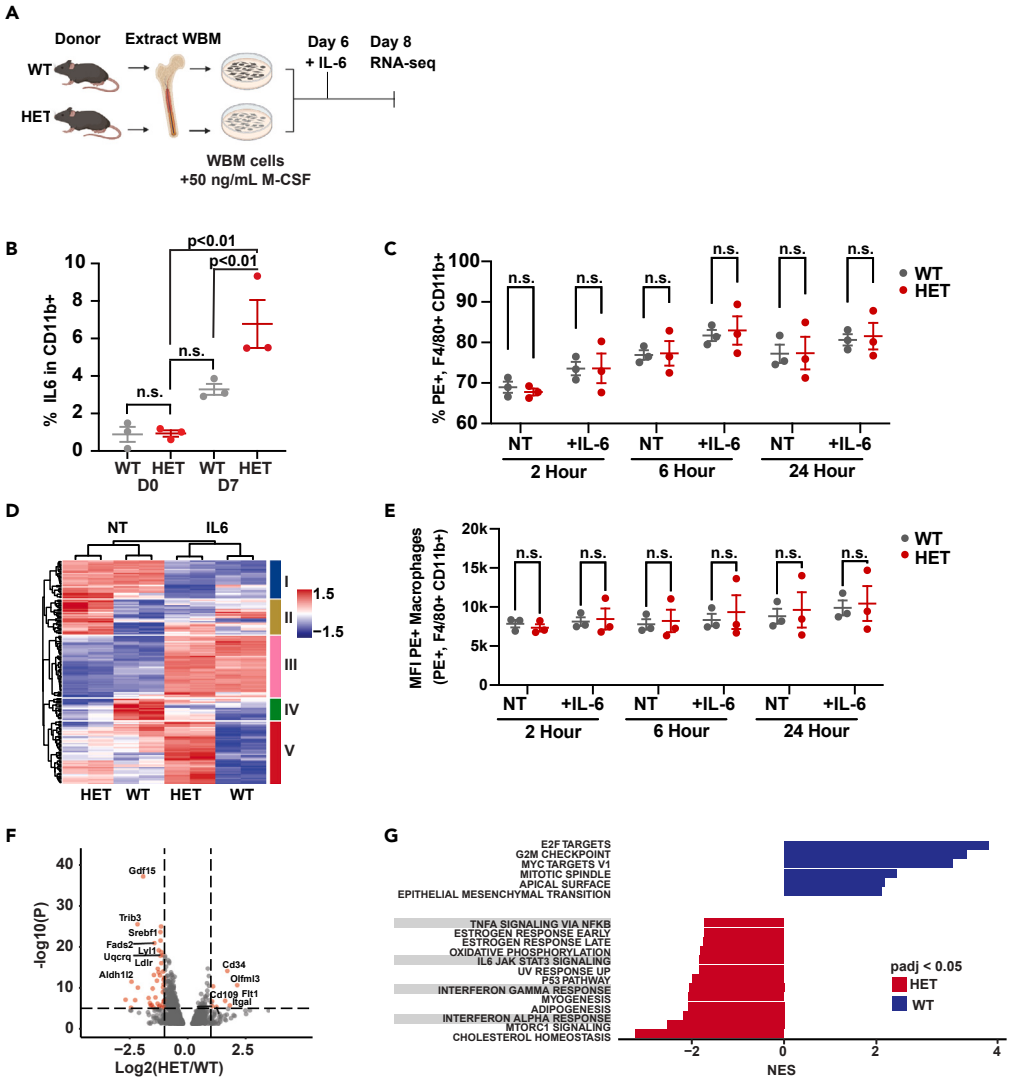

Figure 5. IL-6 exposure reinforces pro-inflammatory pathways in HET bone marrow-derived macrophages

(A) Experimental design. Bone marrow-derived cells from 2-month-old WT or HET (n = 3 per condition) were plated and treated with 10 μg MCSF for 7 days. Cells were then treated with IL-6 at X concentration for an additional 2 days to mimic growth under inflammatory stimulus.

(B) Flow-cytometric quantification of IL-6 using fluorescent antibody crosslinking of *in vitro* differentiated CD11b cells as denoted from day 0 of bone marrow isolation (NT) to day 7 of differentiation. Significance was determined using one-way ANOVA. Data are represented as mean ± SEM.

(C) Phagocytic activity of *in vitro* differentiated WT and HET cells at day 7 of differentiation with or without IL-6 treatment (added on day 6). On day 7 cells were incubated with PE + magnetic beads for the denoted time points and following phagocytic activity was measured. Macrophages were gated based on CD11b+, F4/80+ and incorporation of the PE + beads was then determined. Two-way ANOVA was used to determine statistical significance. Data are represented as mean ± SEM.

(D) Heatmap of the top 200 most variable genes across all samples. Genes were subset by expression patterns across conditions (red indicates higher expression, blue indicates lower expression). Group I (blue) includes genes that were upregulated in NT samples; Group II (gold) indicates genes upregulated only in HET_NT samples; Group III (pink) indicates genes upregulated upon treatment by IL-6; Group IV (green) indicates genes upregulated in WT_NT only; Group V (red) indicates genes that were upregulated in HET_NT and were further upregulated in HET_IL-6 samples. Only the top 200 variable genes are shown, subsetting and testing were performed using the full dataset of expressed genes.

(E) Mean fluorescence intensity (MFI) of the cells from (i). two-way ANOVA was used to determine statistical significance. Data are represented as mean ± SEM.

(F) Differential transcript expression from mature F4/80 macrophages as described in (G) and treated with IL-6. Bulk RNA-seq was performed. Red dots indicate transcripts with p value <0.005 and fold change > 2-fold. Significance testing was performed using Bejamini-Hochberg method to correct p values for multiple hypothesis testing.

(G) GSEA analysis for the hallmark pathways gene sets from MSigDB on IL-6-treated WT versus HET macrophages. Red and blue bars (HET and WT respectively) indicate significantly enriched pathways determined by GSEA normalized ES. Adjusted p value < 0.05.

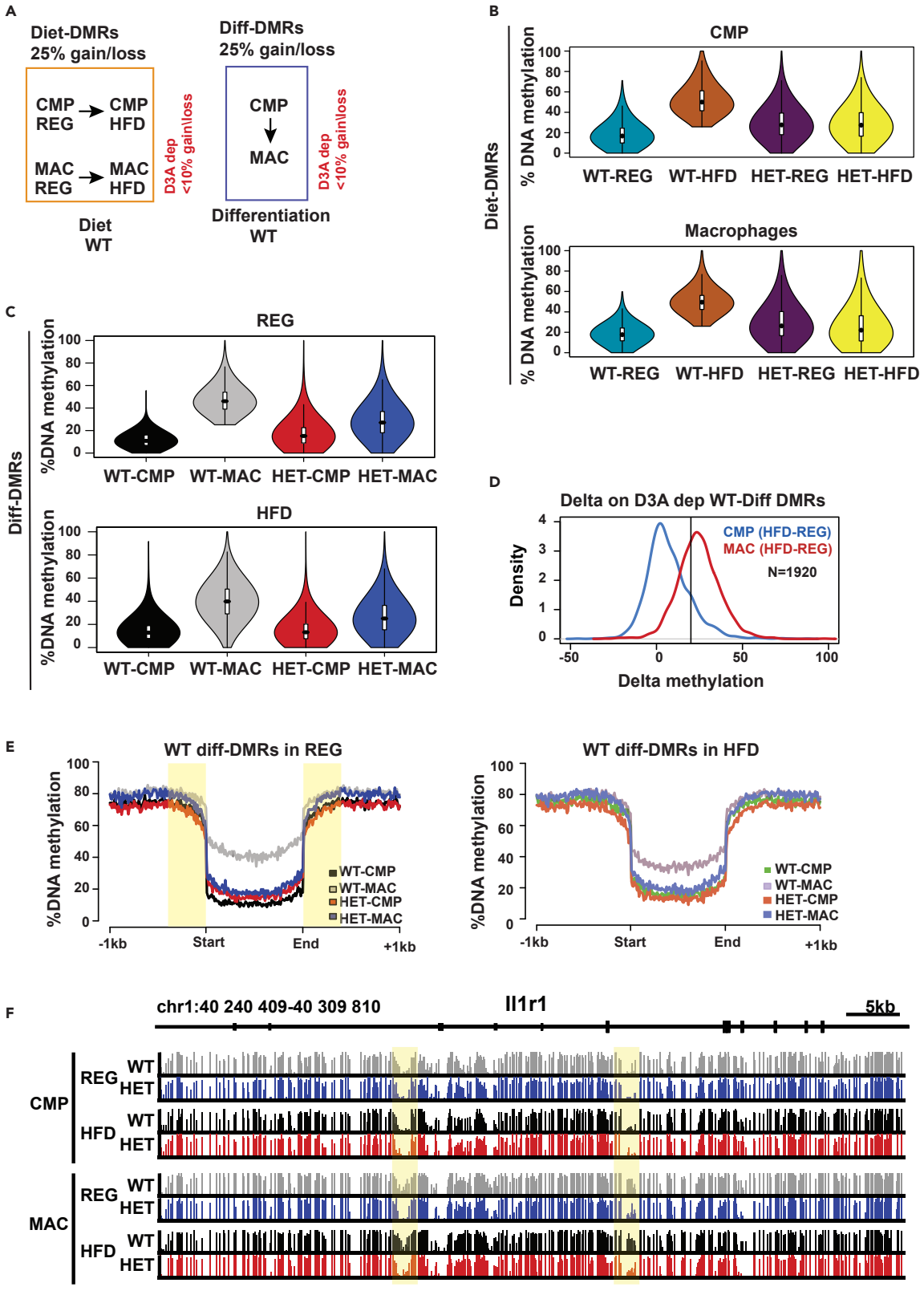
A
Diet-DMRs
25% gain/loss
CMP REG → CMP HFD
MAC REG → MAC HFD
D3A dep <10% gain\loss
Diet WT
Diff-DMRs
25% gain/loss
CMP → MAC
D3A dep <10% gain\loss
Differentiation WT
B
CMP
% DNA methylation
Diet-DMRs
WT-REG WT-HFD HET-REG HET-HFD
Macrophages
% DNA methylation
WT-REG WT-HFD HET-REG HET-HFD
C
REG
Diff-DMRs
%DNA methylation
WT-CMP WT-MAC HET-CMP HET-MAC
HFD
%DNA methylation
WT-CMP WT-MAC HET-CMP HET-MAC
D
Delta on D3A dep WT-Diff DMRs
CMP (HFD-REG)
MAC (HFD-REG)
N=1920
Density
Delta methylation
E
WT diff-DMRs in REG
%DNA methylation
WT-CMP
WT-MAC
HET-CMP
HET-MAC
-1kb Start End +1kb
WT diff-DMRs in HFD
%DNA methylation
WT-CMP
WT-MAC
HET-CMP
HET-MAC
-1kb Start End +1kb
F
chr1:40 240 409-40 309 810
Il1r1
5kb
CMP
REG WT HET
HFD WT HET
MAC
REG WT HET
HFD WT HET

Figure 6. Myeloid progenitors with reduced DNMT3A lack are unable to gain DNA methylation at critical gene regulatory loci

(A) Schematic strategy to define differentially methylated regions (DMRs) as defined for WT- and HET-derived common myeloid progenitors (CMPs) and adipose tissue-isolated macrophages (MACs) 6 moths post-transplant from recipients fed regular diet (REG) or high-fat diet (HFD). Diet-DMRs are defined as regions that gain/loss (~25%) methylation in HFD compared to REG for CMP or MAC. DNMT3A-dependent (D3a dep) Diet-DMRs are regions that had little change (<10%) in HET HFD compared to REG. Differentiation DMRs (Diff-DMRs) are defined as regions that gain/loss (~25%) methylation across differentiation from CMP to MAC. DNMT3A-dependent (D3a dep) Diff-DMRs are regions that had little change (<10%) across differentiation in HET samples.

(B) Violin plot of mean methylation for hypermethylated Diet-DMRs and their mean methylation in WT and HET CMP and macrophages. Boxplots indicate +/− SE mean.

(C) Violin plot of mean methylation for hypermethylated Diff-DMRs and their mean methylation in WT and HET CMP and macrophages. Boxplots indicate +/− SE mean.

(D) Histogram displaying change in mean methylation in HFD compared to regular diet of D3a-dependent Diff-DMRs. These regions were defined when comparing MAC REG to CMP REG. We then calculated mean difference in DNA methylation in HFD compared to REG in either CMPs (blue) or MAC (red). A rightward shift in the line indicates a gain of methylation in HFD for the same loci that gain methylation in differentiation.

(E) Mean methylation +/1 1 kb from D3a-dependent Diff-DMRs. Methylation difference in edges is marked with yellow box (left). For the same regions defined in (e) we plotted mean methylation +/1 1 kb in HFD samples (right).

(F) Whole-genome DNA methylation track from WT and HET cells. Vertical yellow boxes indicate regions that gain DNA methylation during differentiation in WT-CMPs compared to MAC but fail to gain similar degree of methylation in HET cells.

regions that were impacted by HFD as Diet differentially methylated regions (Diet-DMRs, n = 753) and then divided the regions as Diet-hypermethylated (>25% gain) or Diet-hypomethylated (>25% loss) based on WT-CMP REG compared to WT-CMP HFD (Figure 6A; Figure S7A). Similarly, we defined Diet-DMRs for macrophages by comparing WT-MAC on REG compared to WT-MAC HFD (n = 658, Figure S7A). When we similarly calculated Diet-DMRs in HET CMP or MAC, we noticed that the total number of DMRs was lower compared to WT cells (n = 423 for CMP, n = 523 for MAC). As the role of DNMT3A is to establish the DNA methylation *de novo*, we hypothesized that regions that *gained* methylation in WT (i.e., became hypermethylated with diet) would be fewer in the HET. Remarkably we found that for both CMP and MAC most of these regions (~60%) did not gain similar levels of DNA methylation in HET cells. These results indicate that methylation gain in HFD for these loci is mostly DNMT3A dependent.

Next, we examined changes to DNA methylation across *differentiation* state (Diff-DMRs), regardless of diet, by comparing WT-CMP to WT-MAC in REG (Figures 6D and 6E). We identified 4,522 regions for REG which became differentially methylated across differentiation in WT-MAC compared to WT-CMP. When we performed the same analysis for the HFD condition, we found 4,359 regions. Thus, the differentiation state led to more methylation changes and DMRs than diet. From Diff-DMRs, we then distinguished Diff-hyper (>25% gain) and Diff-hypo (>25% loss). Strikingly, reduced DNMT3A in HET cells affected Diff-DMRs even more profoundly than HFD, with the total number of HET Diff-DMRs (~4,000) being significantly higher compared to HET-HFD DMRs (~800) (Figures S7B and S7C). Importantly, many regions (~44%) which gained methylation during differentiation of WT cells did not gain DNA methylation in the differentiation of HET cells from CMP to MAC in REG or HFD, suggesting that methylation gain during differentiation for these regions is DNMT3A dependent (Figure 6C). These results also show that differentiation leads to more profound methylation changes relative to diet, but that DNMT3A plays a major role in both contexts.

We then considered the interaction between differentiation and HFD, examining whether HFD led to methylation changes in a subset of regions that were also impacted by differentiation. We defined CMP to MAC Diff-DMRs in WT cells on REG diet (n = 1,920) and examined how HFD impacted methylation in these regions. We calculated delta methylation in WT HFD-CMP compared to REG-CMP and in WT HFD-MAC compared to REG-MAC (Figure 6B). A large number of regions in CMPs showed an increase in DNA methylation in HFD similar to their behavior during differentiation. This was even more striking in MACs. When we examined genes and pathways associated with these regions, we found that HFD mostly reshaped DNA methylation in a subset of loci that are also modified by DNMT3A during differentiation (Figure S7D). There was marked impact on stem cell genes such as *Hoxa9*, and inflammatory-related pathways, such as *Il1ra1* (Figure 6F; Figures S7D and S7E).

By looking at the pattern of methylation gain in MAC compared to CMP, we noticed that the DNMT3A-dependent methylation gain is across the center and edges of the HMRs. To examine this more broadly, we calculated the average methylation up- and downstream to the Diff-DMRs as defined for WT-CMP in REG. Indeed, during differentiation, methylation is mostly gained at the center of the HMR and very modestly at the edges. However, in HET MAC there is no gain in the transition from CMP to MAC in the center of the HMR, and very modest change at the edges (Figure 6E). Interestingly, analysis in the HFD condition of the regions affected by differentiation revealed similar methylation gain patterns albeit milder. These findings suggest that, as CMPs differentiate to MAC progeny, there is distinct DNMT3A-dependent methylation gain. This gain is significantly lacking in HET MAC compared to WT or HET CMP. Moreover, DNMT3A-dependent modulation of DNA methylation in HFD occurs at largely overlapping loci.

Together with our scRNA analysis and phenotypic characterization, these data indicate that reduced DNMT3A impedes the suppression of pro-inflammatory and stem cell genes that occurs during differentiation. Intriguingly, HFD acts on a subset of loci that are also regulated during normal differentiation and therefore partly recapitulates this regulation on pro-inflammatory activation that occurs in HET-derived progenitors.

DISCUSSION

In this study, we demonstrate that HET loss of *Dnmt3a* in the hematopoietic system increases inflammation and accelerates weight gain of recipient mice. Our findings show that *Dnmt3a*-HET-derived immune cells generate a higher proportion of pro-myeloid cells, specifically

macrophages, particularly in the context of HFD. In mice, HFD impairs glucose tolerance and reduces insulin-mediated glucose metabolism.[30] Here, we link the increased production of myeloid progenitors with higher infiltration of *Dnmt3a*-HET pro-inflammatory macrophages into adipose tissue and pancreatic islets, which occurs more profoundly in HFD than in REG. We further show that this increase in tissue macrophages in HFD correlates with a decrease in insulin-producing cells and perturbed regulation of glucose absorbance, therefore linking dysregulated immune cell production to metabolism and weight gain. Overall, our data suggest a mechanism that links diet and obesity and DNMT3A-mediated CH.

Our findings are supported by recent studies of the UK Biobank, which established a link between obesity and high body mass index (BMI) to CH and increased risk for myeloid-driven leukemia.[31,32]Similarly, studies on overweight or obese individuals from the 300 OB cohort demonstrate an increased association with *DNMT3A* and *TET2* mutations, suggesting a link between weight gain and CH.[33] Additionally, studies of *Dnmt3a* haploinsufficiency on a background of the *Ob/Ob* mice, which develop early obesity, showed that these mice developed myeloproliferative neoplasm-like phenotype, splenomegaly, increased heart weight and glucose levels, and increased frequency of mature myeloid cells compared to control mice.[34] Similarly, we also found that weight gain, albeit from HFD in our model, also led to increased spleen size, leukemia development, and overall shorter lifespan in HET recipients compared to controls.

With regard to diet, our study highlights that HFD induces inflammation both in the whole organism and in the infiltration of macrophages into specific tissues. We discovered that even on a regular diet, *Dnmt3a*-HET bone marrow leads to a preferential increase of macrophages, either tissue resident or circulating, to specific sites such as spleen and pancreas. Furthermore, our findings reveal that HFD amplifies the baseline pro-inflammatory signaling, glucose intolerance, and macrophage infiltration in mice with *Dnmt3a*-HET bone marrow, suggesting a synergistic contribution to the development of CH. It remains to be determined whether this increase in macrophages is due to CMP expansion that leads to more macrophages, or due to altered paracrine signaling from peripheral tissues that either attract more HET-derived macrophages or lead to more macrophage differentiation.

On a molecular level, to understand how the methyltransferase activity of DNMT3A impacts macrophage differentiation, we defined impact of *Dnmt3a* partial loss on gene expression and DNA methylation of CMP and macrophages from REG and HFD. Transcriptionally, *Dnmt3a*-HET immune cells either isolated from adipose tissue or differentiated *in vitro* displayed increased pro-inflammatory transcriptional signatures and upregulated key cytokine pathways including IL-6, IL1, and TNF-α. Also, transcriptional signatures from *Dnmt3a*-HET immune cells from mice on a regular diet have signatures similar to WT-derived cells under HFD, suggesting that loss of a single copy of *Dnmt3a* leads to a pro-inflammatory cellular state similar to the effect of HFD on WT cells.

Our DNA methylation analyses revealed that with reduced DNMT3A HET cells failed to methylate key loci throughout the genome either during differentiation from CMP to macrophage or in response to HFD. These sites are enriched for genes regulating stemness as well as inflammation, consistent with a sustained stem-like cellular state, and upregulation of inflammatory pathways including TNF-α, IL1, and IL-6. Interestingly, a great number of loci that gain methylation during differentiation from CMP to macrophages in WT cells also gain moderate methylation in HFD. These observations suggest that, in the context of a stressor like HFD, *Dnmt3a*-HET cells are preferentially adapted due to this pro-inflammatory priming from CMP to macrophages. Previously our lab has shown that complete loss (inducible homozygous knockout) of DNMT3A in HSCs reshapes the DNA methylation landscape,[9,12] but a direct comparison with mono-allelic (HET) loss of DNMT3A in HSCs has not been performed. To better understand how DNA methylation patterns influence HSC differentiation in response to HFD, how DNA methylation patterns are transmitted across differentiation states, and how these affect cellular function, additional analysis would be required.

IL-6 and IL-1 are both cytokines that are elevated in CH, and those same cytokines are also increased in overweight and obese individuals.[33,35] Our results show that HFD elevates levels of IL-6 in plasma and in immune cells, and that *Dnmt3a*-HET cells upregulate IL-6-associated pathways even in the absence of HFD. Thus, increased IL-6 combined with excess dietary fat promotes an inflammatory milieu that aggravates the effects of mutant *DNMT3A* immune cells. Another recent study showed mouse models of *DNMT3A*^{Mut} HSPCs exposed to fatty bone marrow exhibited activated inflammatory signaling through IL-6 and IFN gamma.[36] In these mice, treatment with anti-IL-6 antibodies reduced the selective advantage of Dnmt3a-mutant HSCs. Human population studies also have identified a link between *DNMT3A*-associated CH and IL-6 signaling. In individuals with *DNMT3A*-CH, individuals with a DNMT3A mutation and a variant of the IL-6 receptor (*IL6R*) that disrupts IL-6 signaling had reduced risk of cardiovascular disease.[35] These studies suggest that IL-6 may be a viable target to abrogate the effects of *DNMT3A*-CH.

Activation of IL-6 and TNF-α pathways in adipose tissues is associated with obesity-related insulin resistance.[37] Here we correlated *Dnmt3a*-HET macrophages in the pancreas with a reduction in total insulin-secreting cells and glucose tolerance, suggesting an interaction between *Dnmt3a*-HET bone marrow and HFD. Considerable evidence in both human and animal studies supports the inflammatory origins of obesity and diabetes. In addition, increased tissue infiltration by macrophages following HFD promotes local and systemic inflammation, impairing insulin signaling and contributing to weight gain.[38,39] While we observed reduced insulin production and glucose clearance in HET-transplanted mice, this was not at levels typically associated with insulin resistance and obesity. Inhibited glucose uptake, however, increases fat production and affects insulin resistance over time.[40] We therefore postulate that *Dnmt3a*-mediated CH and inflammation within metabolic organs due to HFD contribute to weight gain and may be a risk factor for metabolic disorders in humans.

Together, we show that *Dnmt3a*-HET-derived macrophages have increased inflammatory signaling at baseline due to improper DNA methylation, and this priming may give *Dnmt3a*-HET cells an advantage over WT-derived cells in responding to inflammation. We find that *Dnmt3a*-HET hematopoietic cells expand in the blood regardless of diet, but HFD increases weight gain, tissue infiltration by *Dnmt3a*-HET immune cells, pancreatic dysfunction, and pro-inflammatory signaling in HET-transplanted mice. Overall, our findings highlight how diet and *Dnmt3a*-HET bone marrow influence tissue microenvironments and impact organ function over time.

Limitations of the study

Our manuscript provides the first evidence supporting the role of DNMT3A in regulating myeloid differentiation in the context of HFD-mediated inflammation. We also show a correlation between myeloid cell expansion, glucose tolerance, and weight gain in recipients of Dnmt3a-HET cells. In the manuscript, we show expansion of the CMP fraction with increased myeloid infiltration into tissues in HFD; however, we are unable to completely delineate between the effects of DNMT3A loss, an HFD, or synergy between them. It will be interesting to perform follow-up studies using transplantation of specific myeloid populations in obesity models as performed using TET2.[34] Intriguingly, we did not observe differences in HET macrophage phagocytic activity. Recent publications using DNMT3A-knockout mice have shown that DNMT3A acts downstream of phagocytosis and is essential for Irk-COX-TGF-β activation upon clearance of apoptotic cells.[41] Similarly, it is plausible that in our model lack of DNMT3A prevents clearance of apoptotic cells in adipose tissue or the pancreas explaining the decrease in insulin-secreting cells. Additional functional macrophage assays would be necessary to support the role of HET macrophages in the increased inflammatory signaling and reduction of insulin secretion observed in Dnmt3a-HET mice with or without HFD. Finally, although we show activation of pro-inflammatory pathways in HET cells in REG diet, we are unable to determine how diet-derived inflammatory signaling further increases inflammatory signaling in the HET cells. We cannot determine whether HET cells are intrinsically responding to diet or are interacting with other factors to exacerbate inflammation.

STAR★METHODS

Detailed methods are provided in the online version of this paper and include the following:

- KEY RESOURCES TABLE
- RESOURCE AVAILABILITY
  - Lead contact
  - Materials availability
  - Data and code availability
- EXPERIMENTAL MODEL AND STUDY PARTICIPANT DETAILS
  - Mouse models
- METHOD DETAILS
  - Cell culture and differentiation of macrophages
  - Mouse hematopoietic progenitor and peripheral blood staining
  - Glucose and insulin tolerance test
  - H&E tissue staining
  - Immunofluorescence in mouse tissue
  - Library preparation and sequencing analysis
- QUANTIFICATION AND STATISTICAL ANALYSIS
  - Statistical analysis
  - Single cell RNA filtering and normalization
  - Mapping to Reference LSK scRNA dataset
  - Integrated dataset clustering and annotation
  - Pseudotime lineage selection and assignment
  - scRNA differential gene expression and pathway enrichment
  - Differential methylation analysis

SUPPLEMENTAL INFORMATION

Supplemental information can be found online at https://doi.org/10.1016/j.isci.2024.109122.

ACKNOWLEDGMENTS

We thank Sean Hartig and Huawei Zhu as well as members of the Goodell Lab for helpful suggestions. We also thank the Baylor College of Medicine Advanced Technology Cores: Genomic and RNA Profiling, Single Cell Genomics, the Cytometry and Cell Sorting, Metabolomics, and Mouse Metabolism and Phenotyping supported in part by grants CA125123, HG006348, HL130249, and RP180672. This work was supported in part by a grant to Baylor College of Medicine from the Howard Hughes Medical Institute through the James H. Gilliam Fellowships for Advanced Study program. In addition, this work was supported by the Baylor College of Medicine Medical Scientist Training Program, as well as NIH grants CA183252, DK092883, AG036695, CA265748, R01HD099252, R01HD098131, HL092332, S10OD023469, S10OD025240, and RP200504.

AUTHOR CONTRIBUTIONS

J.M.R., A.T., and M.A.G. conceived the project, discussed and designed experiments, and wrote the manuscript. J.M.R. and A.T. performed experiments, analyzed data, and wrote the manuscript. J.M.R. performed bioinformatic analyses. L.Z., A. Bortoletto, C.R., C.-W.C., S.M.W.,

A.G.G., R.A., K.R.P., A.N.M., C.V.C., S.G., L.L., M.T.B., and Y.L. performed experiments and analyzed data. T.R., A. Brunet, R.P., and R.E.R. analyzed data and provided resources.

DECLARATION OF INTERESTS

The authors declare no competing interests.

Received: July 14, 2022
Revised: December 11, 2023
Accepted: January 31, 2024
Published: February 5, 2024

REFERENCES

1. Libby, P., Sidlow, R., Lin, A.E., Gupta, D., Jones, L.W., Moslehi, J., Zeiher, A., Jaiswal, S., Schulz, C., Blankstein, R., et al. (2019). Clonal Hematopoiesis: Crossroads of Aging, Cardiovascular Disease, and Cancer: JACC Review Topic of the Week. J. Am. Coll. Cardiol. *74*, 567–577. https://doi.org/10.1016/j.jacc.2019.06.007.
2. Luis, T.C., Wilkinson, A.C., Beerman, I., Jaiswal, S., and Shlush, L.I. (2019). Biological implications of clonal hematopoiesis. Exp. Hematol. *77*, 1–5. https://doi.org/10.1016/j.exphem.2019.08.004.
3. Bick, A.G., Weinstock, J.S., Nandakumar, S.K., Fulco, C.P., Bao, E.L., Zekavat, S.M., Szeto, M.D., Liao, X., Leventhal, M.J., Nasser, J., et al. (2020). Inherited causes of clonal haematopoiesis in 97,691 whole genomes. Nature *586*, 763–768. https://doi.org/10.1038/s41586-020-2819-2.
4. Jaiswal, S., Fontanillas, P., Flannick, J., Manning, A., Grauman, P.V., Mar, B.G., Lindsley, R.C., Mermel, C.H., Burtt, N., Chavez, A., et al. (2014). Age-related clonal hematopoiesis associated with adverse outcomes. N. Engl. J. Med. *371*, 2488–2498. https://doi.org/10.1056/NEJMoa1408617.
5. Genovese, G., Kähler, A.K., Handsaker, R.E., Lindberg, J., Rose, S.A., Bakhoum, S.F., Chambert, K., Mick, E., Neale, B.M., Fromer, M., et al. (2014). Clonal hematopoiesis and blood-cancer risk inferred from blood DNA sequence. N. Engl. J. Med. *371*, 2477–2487. https://doi.org/10.1056/NEJMoa1409405.
6. Okano, M., Bell, D.W., Haber, D.A., and Li, E. (1999). DNA methyltransferases Dnmt3a and Dnmt3b are essential for de novo methylation and mammalian development. Cell *99*, 247–257. https://doi.org/10.1016/s0092-8674(00)81656-6.
7. Zhang, X., Jeong, M., Huang, X., Wang, X.Q., Wang, X., Zhou, W., Shamim, M.S., Gore, H., Himadewi, P., Liu, Y., et al. (2020). Large DNA Methylation Nadirs Anchor Chromatin Loops Maintaining Hematopoietic Stem Cell Identity. Mol. Cell *78*, 506–521.e6. https://doi.org/10.1016/j.molcel.2020.04.018.
8. Gu, T., Hao, D., Woo, J., Huang, T.W., Guo, L., Lin, X., Guzman, A.G., Tovy, A., Rosas, C., Jeong, M., et al. (2022). The disordered N-terminal domain of DNMT3A recognizes H2AK119ub and is required for postnatal development. Nat. Genet. *54*, 625–636. https://doi.org/10.1038/s41588-022-01063-6.
9. Challen, G.A., Sun, D., Jeong, M., Luo, M., Jelinek, J., Berg, J.S., Bock, C., Vasanthakumar, A., Gu, H., Xi, Y., et al. (2011). Dnmt3a is essential for hematopoietic stem cell differentiation. Nat. Genet. *44*, 23–31. https://doi.org/10.1038/ng.1009.
10. Chen, T., Ueda, Y., Dodge, J.E., Wang, Z., and Li, E. (2003). Establishment and maintenance of genomic methylation patterns in mouse embryonic stem cells by Dnmt3a and Dnmt3b. Mol. Cell. Biol. *23*, 5594–5605. https://doi.org/10.1128/mcb.23.16.5594-5605.2003.
11. Tovy, A., Rosas, C., Gaikwad, A.S., Medrano, G., Zhang, L., Reyes, J.M., Huang, Y.H., Arakawa, T., Kurtz, K., Conneely, S.E., et al. (2022). Perturbed hematopoiesis in individuals with germline DNMT3A overgrowth Tatton-Brown-Rahman syndrome. Haematologica *107*, 887–898. https://doi.org/10.3324/haematol.2021.278990.
12. Challen, G.A., Sun, D., Mayle, A., Jeong, M., Luo, M., Rodriguez, B., Mallaney, C., Celik, H., Yang, L., Xia, Z., et al. (2014). Dnmt3a and Dnmt3b have overlapping and distinct functions in hematopoietic stem cells. Cell Stem Cell *15*, 350–364. https://doi.org/10.1016/j.stem.2014.06.018.
13. Jeong, M., Park, H.J., Celik, H., Ostrander, E.L., Reyes, J.M., Guzman, A., Rodriguez, B., Lei, Y., Lee, Y., Ding, L., et al. (2018). Loss of Dnmt3a Immortalizes Hematopoietic Stem Cells In Vivo. Cell Rep. *23*, 1–10. https://doi.org/10.1016/j.celrep.2018.03.025.
14. Challen, G.A., and Goodell, M.A. (2020). Clonal hematopoiesis: mechanisms driving dominance of stem cell clones. Blood *136*, 1590–1598. https://doi.org/10.1182/blood.2020006510.
15. Mayle, A., Yang, L., Rodriguez, B., Zhou, T., Chang, E., Curry, C.V., Challen, G.A., Li, W., Wheeler, D., Rebel, V.I., and Goodell, M.A. (2015). Dnmt3a loss predisposes murine hematopoietic stem cells to malignant transformation. Blood *125*, 629–638. https://doi.org/10.1182/blood-2014-08-594648.
16. Ley, T.J., Ding, L., Walter, M.J., McLellan, M.D., Lamprecht, T., Larson, D.E., Kandoth, C., Payton, J.E., Baty, J., Welch, J., et al. (2010). DNMT3A mutations in acute myeloid leukemia. N. Engl. J. Med. *363*, 2424–2433. https://doi.org/10.1056/NEJMoa1005143.
17. Yang, L., Rau, R., and Goodell, M.A. (2015). DNMT3A in haematological malignancies. Nat. Rev. Cancer *15*, 152–165. https://doi.org/10.1038/nrc3895.
18. Florez, M.A., Tran, B.T., Wathan, T.K., DeGregori, J., Pietras, E.M., and King, K.Y. (2022). Clonal hematopoiesis: Mutation-specific adaptation to environmental change. Cell Stem Cell *29*, 882–904. https://doi.org/10.1016/j.stem.2022.05.006.
19. Cobo, I., Tanaka, T., Glass, C.K., and Yeang, C. (2022). Clonal hematopoiesis driven by DNMT3A and TET2 mutations: role in monocyte and macrophage biology and atherosclerotic cardiovascular disease. Curr. Opin. Hematol. *29*, 1–7. https://doi.org/10.1097/MOH.0000000000000688.
20. Fuster, J.J., MacLauchlan, S., Zuriaga, M.A., Polackal, M.N., Ostriker, A.C., Chakraborty, R., Wu, C.L., Sano, S., Muralidharan, S., Rius, C., et al. (2017). Clonal hematopoiesis associated with TET2 deficiency accelerates atherosclerosis development in mice. Science *355*, 842–847. https://doi.org/10.1126/science.aag1381.
21. Abplanalp, W.T., Cremer, S., John, D., Hoffmann, J., Schuhmacher, B., Merten, M., Rieger, M.A., Vasa-Nicotera, M., Zeiher, A.M., and Dimmeler, S. (2021). Clonal Hematopoiesis-Driver DNMT3A Mutations Alter Immune Cells in Heart Failure. Circ. Res. *128*, 216–228. https://doi.org/10.1161/CIRCRESAHA.120.317104.
22. Singer, K., DelProposto, J., Morris, D.L., Zamarron, B., Mergian, T., Maley, N., Cho, K.W., Geletka, L., Subbaiah, P., Muir, L., et al. (2014). Diet-induced obesity promotes myelopoiesis in hematopoietic stem cells. Mol. Metab. *3*, 664–675. https://doi.org/10.1016/j.molmet.2014.06.005.
23. Maharjan, B.R., McLennan, S.V., Yee, C., Twigg, S.M., and Williams, P.F. (2021). The Effect of a Sustained High-Fat Diet on the Metabolism of White and Brown Adipose Tissue and Its Impact on Insulin Resistance: A Selected Time Point Cross-Sectional Study. Int. J. Mol. Sci. *22*, 13639. https://doi.org/10.3390/ijms222413639.
24. Kiran, S., Rakib, A., Kodidela, S., Kumar, S., and Singh, U.P. (2022). High-Fat Diet-Induced Dysregulation of Immune Cells Correlates with Macrophage Phenotypes and Chronic Inflammation in Adipose Tissue. Cells *11*. https://doi.org/10.3390/cells11081327.
25. Weisberg, S.P., McCann, D., Desai, M., Rosenbaum, M., Leibel, R.L., and Ferrante, A.W., Jr. (2003). Obesity is associated with macrophage accumulation in adipose tissue. J. Clin. Invest. *112*, 1796–1808. https://doi.org/10.1172/JCI19246.
26. Khodabandehloo, H., Gorgani-Firuzjaee, S., Panahi, G., and Meshkani, R. (2016). Molecular and cellular mechanisms linking inflammation to insulin resistance and beta-cell dysfunction. Transl. Res. *167*, 228–256. https://doi.org/10.1016/j.trsl.2015.08.011.
27. Aran, D., Looney, A.P., Liu, L., Wu, E., Fong, V., Hsu, A., Chak, S., Naikawadi, R.P., Wolters, P.J., Abate, A.R., et al. (2019). Reference-based analysis of lung single-cell sequencing reveals a transitional profibrotic macrophage. Nat. Immunol. *20*, 163–172. https://doi.org/10.1038/s41590-018-0276-y.

28. Tovy, A., Reyes, J.M., Zhang, L., Huang, Y.H., Rosas, C., Daquinag, A.C., Guzman, A., Ramabadran, R., Chen, C.W., Gu, T., et al. (2022). Constitutive loss of DNMT3A causes morbid obesity through misregulation of adipogenesis. Elife *11*, e72359. https://doi.org/10.7554/eLife.72359.
29. Cortez, M., Carmo, L.S., Rogero, M.M., Borelli, P., and Fock, R.A. (2013). A high-fat diet increases IL-1, IL-6, and TNF-alpha production by increasing NF-kappaB and attenuating PPAR-gamma expression in bone marrow mesenchymal stem cells. Inflammation *36*, 379–386. https://doi.org/10.1007/s10753-012-9557-z.
30. Santoro, A., McGraw, T.E., and Kahn, B.B. (2021). Insulin action in adipocytes, adipose remodeling, and systemic effects. Cell Metab. *33*, 748–757. https://doi.org/10.1016/j.cmet.2021.03.019.
31. Komic, L., Kumric, M., Urlic, H., Rizikalo, A., Grahovac, M., Kelam, J., Tomicic, M., Rusic, D., Ticinovic Kurir, T., and Bozic, J. (2023). Obesity and Clonal Hematopoiesis of Indeterminate Potential: Allies in Cardiovascular Diseases and Malignancies. Life *13*. https://doi.org/10.3390/life13061365.
32. Bhattacharya, R., Zekavat, S.M., Uddin, M.M., Pirruccello, J., Niroula, A., Gibson, C., Griffin, G.K., Libby, P., Ebert, B.L., Bick, A., and Natarajan, P. (2021). Association of Diet Quality With Prevalence of Clonal Hematopoiesis and Adverse Cardiovascular Events. JAMA Cardiol. *6*, 1069–1077. https://doi.org/10.1001/jamacardio.2021.1678.
33. Tercan, H., Van Deuren, R.C., Schraa, K., Horst, R.T., Van Den Munckhof, I.C., Bekkering, S., Rutten, J.H., Netea, M.G., Joosten, L.A.B., Hoischen, A., and Riksen, N.P. (2021). Clonal hematopoiesis and inflammation in obesity. Atherosclerosis *331*, e113. https://doi.org/10.1016/j.atherosclerosis.2021.06.333.
34. Pasupuleti, S.K., Ramdas, B., Burns, S.S., Palam, L.R., Kanumuri, R., Kumar, R., Pandhiri, T.R., Dave, U.P., Yellapu, N.K., Zhou, X., et al. (2023). Obesity-induced inflammation exacerbates clonal hematopoiesis. J. Clin. Invest. *133*, e163968. https://doi.org/10.1172/JCI163968.
35. Bick, A.G., Pirruccello, J.P., Griffin, G.K., Gupta, N., Gabriel, S., Saleheen, D., Libby, P., Kathiresan, S., and Natarajan, P. (2020). Genetic Interleukin 6 Signaling Deficiency Attenuates Cardiovascular Risk in Clonal Hematopoiesis. Circulation *141*, 124–131. https://doi.org/10.1161/CIRCULATIONAHA.119.044362.
36. Zioni, N., Bercovich, A.A., Chapal-Ilani, N., Bacharach, T., Rappoport, N., Solomon, A., Avraham, R., Kopitman, E., Porat, Z., Sacma, M., et al. (2023). Inflammatory signals from fatty bone marrow support DNMT3A driven clonal hematopoiesis. Nat. Commun. *14*, 2070. https://doi.org/10.1038/s41467-023-36906-1.
37. Kern, P.A., Ranganathan, S., Li, C., Wood, L., and Ranganathan, G. (2001). Adipose tissue tumor necrosis factor and interleukin-6 expression in human obesity and insulin resistance. Am. J. Physiol. Endocrinol. Metab. *280*, E745–E751. https://doi.org/10.1152/ajpendo.2001.280.5.E745.
38. Haase, J., Weyer, U., Immig, K., Klöting, N., Blüher, M., Eilers, J., Bechmann, I., and Gericke, M. (2014). Local proliferation of macrophages in adipose tissue during obesity-induced inflammation. Diabetologia *57*, 562–571. https://doi.org/10.1007/s00125-013-3139-y.
39. Zatterale, F., Longo, M., Naderi, J., Raciti, G.A., Desiderio, A., Miele, C., and Beguinot, F. (2019). Chronic Adipose Tissue Inflammation Linking Obesity to Insulin Resistance and Type 2 Diabetes. Front. Physiol. *10*, 1607. https://doi.org/10.3389/fphys.2019.01607.
40. Czech, M.P. (2017). Insulin action and resistance in obesity and type 2 diabetes. Nat. Med. *23*, 804–814. https://doi.org/10.1038/nm.4350.
41. Ampomah, P.B., Cai, B., Sukka, S.R., Gerlach, B.D., Yurdagul, A., Jr., Wang, X., Kuriakose, G., Darville, L.N.F., Sun, Y., Sidoli, S., et al. (2022). Macrophages use apoptotic cell-derived methionine and DNMT3A during efferocytosis to promote tissue resolution. Nat. Metab. *4*, 444–457. https://doi.org/10.1038/s42255-022-00551-7.
42. Hao, Y., Hao, S., Andersen-Nissen, E., Mauck, W.M., 3rd, Zheng, S., Butler, A., Lee, M.J., Wilk, A.J., Darby, C., Zager, M., et al. (2021). Integrated analysis of multimodal single-cell data. Cell *184*, 3573–3587.e29. https://doi.org/10.1016/j.cell.2021.04.048.
43. Street, K., Risso, D., Fletcher, R.B., Das, D., Ngai, J., Yosef, N., Purdom, E., and Dudoit, S. (2018). Slingshot: cell lineage and pseudotime inference for single-cell transcriptomics. BMC Genomics *19*, 477. https://doi.org/10.1186/s12864-018-4772-0.
44. Ji, Z., and Ji, H. (2016). TSCAN: Pseudo-time reconstruction and evaluation in single-cell RNA-seq analysis. Nucleic Acids Res. *44*, e117. https://doi.org/10.1093/nar/gkw430.
45. Dobin, A., Davis, C.A., Schlesinger, F., Drenkow, J., Zaleski, C., Jha, S., Batut, P., Chaisson, M., and Gingeras, T.R. (2013). STAR: ultrafast universal RNA-seq aligner. Bioinformatics *29*, 15–21. https://doi.org/10.1093/bioinformatics/bts635.
46. Love, M.I., Huber, W., and Anders, S. (2014). Moderated estimation of fold change and dispersion for RNA-seq data with DESeq2. Genome Biol. *15*, 550. https://doi.org/10.1186/s13059-014-0550-8.
47. Krueger, F., and Andrews, S.R. (2011). Bismark: a flexible aligner and methylation caller for Bisulfite-Seq applications. Bioinformatics *27*, 1571–1572. https://doi.org/10.1093/bioinformatics/btr167.
48. Chen, H., Smith, A.D., and Chen, T. (2016). WALT: fast and accurate read mapping for bisulfite sequencing. Bioinformatics *32*, 3507–3509. https://doi.org/10.1093/bioinformatics/btw490.

STAR★METHODS

KEY RESOURCES TABLE

REAGENT or RESOURCE	SOURCE	IDENTIFIER
Antibodies		
PE-Cy7 anti-Mouse Ly-6G	eBioscience	25-5931-82
PE-Cy7 anti-Mouse CD11b	BD Bioscience	552850
PE-Cy7 anti-Mouse B220	BD Bioscience	552772
eFluor 450 anti-Mouse CD4	eBioscience	48-0042-82
eFluor 450 anti-Mouse CD8a	eBioscience	48-0081-82
eFluor 450 anti-Mouse B220	eBioscience	48-0452-82
eFluor 450 anti-Mouse TER-119	eBioscience	48-5921-82
APC-Cy7 anti-Mouse CD117	BioLegend	135136
PE-Cy7 anti-Mouse Sca-1	eBioscience	25-5981-82
BV510 anti-mouse CD48	BD Bioscience	563536
PE anti-Mouse CD150	eBioscience	12-1502-82
APC anti-Mouse CD45.1	eBioscience	17-0453-82
FITC anti-Mouse CD45.2	eBioscience	11-0454-82
PE anti-Mouse CD16/32	eBioscience	12-0161-82
FITC anti-Mouse CD127	eBioscience	11-1271-82
PB anti-Mouse CD45.2	eBioscience	48-0454-82
APC anti-Mouse CD34	BioLegend	119309
Mouse IgG1 anti-insulin	Santa Cruz	sc-8033
Rat anti-F4/80	Abcam	ab6640
Goat anti-mouse IgG1 Alexa Fluor 488	Thermo Fisher	A-21121
Goat anti-rat Alexa Fluor 594	Thermo Fisher	A-11007
Biological samples		
Mouse bone marrow	This study	N/A
Mouse *in vitro* differentiated macrophages	This study	N/A
Chemicals, peptides, and recombinant proteins		
Mouse CD117 MicroBeads	Miltenyi	130-091-224
Recombinant Murine IL-6	PeproTech	216-16
M-CSF	ThermoFisher	PMC2044
High fat diet	Research Diets Inc.	D12451
Critical commercial assays		
AllPrep DNA/RNA Micro Kit	Qiagen	80284
IL-6 ELISA Kit	Abcam	ab178013
TruSeq® Stranded mRNA Library Prep	Illumina	20020594
CUTANA™ DNA Purification Kit	EpiCypher	14-0050
NEBNext® Ultra™ II DNA Library Prep Kit for Illumina	New England Biolabs	E7645
Nextera XT DNA Library Preparation Kit	Illumina	FC-131-1096
DNA Clean & Concentrator	Zymo Research	D4030
Chromium Next GEM Single Cell 3' Kit v3.1	10X Genomics	PN-1000268

(*Continued on next page*)

Continued

REAGENT or RESOURCE	SOURCE	IDENTIFIER
Deposited data		
RNA-sequencing data	This study	GEO: GSE208075
Whole genome bisulfite sequencing data	This study	GEO: GSE208075
Single cell RNA-seq data	This study	GEO: GSE208075
Experimental models: Organisms/strains		
Mice: CD45.1 (B6.SJL-Ptprcapepcb/Boyj)	Jackson Laboratory	Stock #002014
Germline heterozygous knockout DNMT3A	Tovy et al.[11]	N/A
Software and algorithms		
ImageJ (v1.53t)		https://imagej.net/
Adobe Illustrator	Adobe	https://www.adobe.com/products/illustrator.html
R (v4.3.1)	R-project	https://www.r-project.org/
Python (v3.10.9)	Python Software Foundation	https://www.python.org/
GraphPad PRISM (v8.4.2)	Dotmatics	https://www.graphpad.com/features
FACSdiva (v8.0.1)	BD Biosciences	https://www.bdbiosciences.com/en-us/products/software/instrument-software/bd-facsdiva-software
FlowJo (v10.7.1)	BD Biosciences	https://www.bdbiosciences.com/en-us/products/software/flowjo-v10-software
Cell Ranger (v3.1.0)	10X Genomics	https://www.10xgenomics.com/support/software/cell-ranger
Seurat (v4.0.4)	Hao et al.[42]	https://satijalab.org/seurat/
SingleR (v1.0)	Aran et al.[27]	https://code.bioconductor.org/browse/SingleR/tree/RELEASE_3_18/
Slingshot (v2.10.0)	Street et al.[43]	https://github.com/kstreet13/slingshot
TSCAN	Ji et al.[44]	https://github.com/zji90/TSCAN
STAR (v020201)	Dobin et al.[45]	https://github.com/alexdobin/STAR
DESeq2 (V1.36.0)	Love et al.[46]	https://bioconductor.org/packages/release/bioc/html/DESeq2.html
Bismark	Babraham Institute	https://www.bioinformatics.babraham.ac.uk/projects/bismark/
Integrated Genomics Viewer	Broad Institute	https://igv.org/doc/desktop/
HOMER	UCSD	http://homer.ucsd.edu/homer/motif/

RESOURCE AVAILABILITY

Lead contact

- Further information and requests of reagents can be directed to and fulfilled by the lead contact, Margaret Goodell (goodell@bcm.edu).

Materials availability

- This study did not generate new unique reagents.

Data and code availability

- Whole genome bisulfite sequencing data, bulk and single cell RNA-seq data have been deposited at GEO and are publicly available as of the date of publication.

- No original code was developed for this study.
- Any additional information required to reanalyze the data reported in this paper is available from the lead contact upon request.

EXPERIMENTAL MODEL AND STUDY PARTICIPANT DETAILS

Mouse models

All mice were housed in AAALAC-accredited, specific-pathogen-free animal care facilities at Baylor College of Medicine, and all procedures were approved by the BCM Institutional Animal Care and Use Committee. All mice were immune-competent and healthy prior to the experiments described. Both male and female mice were used in studies, unless indicated. Mice were bred and maintained at regular housing temperatures (23°C) and 12-h light/12-h dark cycle starting at 7:00 a.m. Animals had *ad libitum* access to water and either high fat (45 kcal % fat, Research Diets Inc.) or chow diet, depending on the study being performed. For physiological fasting experiments, mice were fasted from 7:00 p.m. to 7:00 a.m. Bone marrow donor mice were 2 months of age at the time of collection. All other mice were between 8 and 24 months of age as indicated with associated experiments.

METHOD DETAILS

Cell culture and differentiation of macrophages

Bone marrow was collected from 3 male mice per genotype at 13 weeks of age (Day 0). Whole bone marrow was plated at 4 x10^5 cells per 10 cm dish in macrophage differentiation medium (DMEM, 10% FBS, 1x GlutaMAX, 1x non-essential amino acids, 1x sodium pyruvate, 1x penicillin/streptomycin, 1 μM beta-mercaptoethanol, and 50 ng/mL M-CSF) until Day 6. On Day 6, 10 ng/mL IL-6 was added to the appropriate samples. On Day 8, macrophages were collected for RNA isolation using the RNeasy mini kit (Qiagen).

Mouse hematopoietic progenitor and peripheral blood staining

Peripheral blood was collected into a tube with anti-coagulant dextran solution and following separation of layers, the top layer containing white blood cells was transferred to a collection tube for RBC lysis for 15 min. Cells were then washed and stained for 15 min for the described populations as previously described by our lab. Cells were analyzed by flow cytometry (LSRII, Becton Dickinson) with the FACSdiva software (BD Biosciences). A minimum of 10,000 cells was analyzed per sample, and data was visualized using the FlowJo software (FlowJo, LLC). Lineage markers were used for B-cells ($CD4^+$, Cd11b+), T-cells ($CD4^+$, Cd11b-), and Myeloid (Cd11b+, $CD4^-$) cells as previously described.

Glucose and insulin tolerance test

Mice were fasted for 12 h, following they received IP injection of 20% glucose per kg, for glucose tolerance test or 0.15 IU/kg insulin for insulin tolerance test. Blood samples are collected prior to and after the injection at time 0, 15, 30, 60, and 120 min via tail vein bleeding. Blood levels of glucose are measured based on using a glucometer. Fasting glucose or insulin levels were measured from plasma by glucose hexokinase assay by using Millipore rat/mouse insulin ELISA kit.

H&E tissue staining

Animals were sacrificed, and tissues for downstream analysis were fixed in 4% buffered formalin and submitted to the Pathology and Histology Core, BCM. Sections were stained with hematoxylin and eosin using standard protocols.

Immunofluorescence in mouse tissue

Pancreatic tissue was equilibrated in a sucrose gradient for cryoprotection and embedded in O.C.T. (Sakura Finetek). Tissue blocks were sectioned at 10 μM thickness and slides were stored at −80°C until staining. For immunofluorescence, slides were warmed to RT, then washed three times with 0.1% Triton-X in PBS (PT) for 5 min each. Blocking (5% goat serum, 1% BSA in PBS) was done for 1 h at RT. Primary antibodies were centrifuged at 15,000 x g for 5 min at 4°C before being diluted in blocking buffer. Slides were incubated overnight at 4°C in primary antibody solutions containing mouse IgG1 anti-insulin (Santa Cruz sc-8033, 1:500) and rat anti-F4/80 (Abcam ab6640, 1:100). After incubation, slides were washed 5 times with PT for 5 min each, then incubated for 2 h at RT with fluorescently-conjugated secondary antibodies (goat anti-mouse IgG1 Alexa Fluor 488 1:500 and goat anti-rat Alexa Fluor 594 1:500) (Fisher). After secondary antibody incubation, slides were washed 5 times with PT for 5 min each and incubated in DAPI (1 μg/mL, Sigma) for 10 min. After three, 5-min washes with PT, slides were mounted and images were visualized using confocal microscopy (LSM 990 confocal microscope: Zeiss, Thornwood, NY, USA).

Library preparation and sequencing analysis

Single cell RNA library preparation

Cells derived from mice receiving HET or WT bone marrow 10-month post-transplant and fed either HFD or REG were used to make single cell RNA libraries using the 10x Genomics Chromium Platform. LSKs ($Lineage^{neg}$ $Sca\text{-}1^{pos}$, $cKit^{pos}$) cells were extracted using bone marrow extraction and FACS procedure as described above. Immune cells from adipose tissue were extracted by dissecting adipose tissue followed by

single cells suspension of tissue, and sorting for CD45$^+$ cells. Cell suspensions were submitted to the Single Cell Genomics Core (BCM) and libraries were prepared according to standard 10X Chromium protocols.

Single-cell RNA library sequencing

Libraries were sequenced on Illumina NovaSeq to an average depth of 54,609 reads per cell to achieve an average of ~75% barcode saturation. Fastqs were generated using 'cellranger mkfastq' (10X Genomics, version 3.1.0, default parameters). Because libraries were generated and sequenced across multiple time points, we applied 'cellranger aggr' to aggregate and normalize libraries across all samples and replicates. Average read depth and barcode saturation were calculated using 'cellranger aggr'.

Bulk RNA sequencing and analysis

RNA was extracted using RNeasy micro kit (Qiagen) and quantified using Nanodrop. We prepared the Truseq stranded mRNA library using the manufacturer's instructions (Illumina). Libraries were sequenced using Nextseq 2000 sequencer. Paired-end RNA-seq reads were mapped to mouse genome (mm10) using STAR. Reads were counted using featureCounts and differential expression was determined using DESeq2.

Whole genome bisulfite sequencing library preparation and analysis

Common myeloid progenitors were sorted from 10-month post-transplant mice and DNA was extracted using DNeasy kit and All Prep DNA/RNA micro kit (Qiagen). DNA was fragmented prior to bisulfite conversation using NEBNext fragmentase kit, following the manufacturer's protocol (NEB). We used 10 ng DNA to prepare WGBS libraries with the Swift-whole genome bisulfite kit according to the manufacturer's instruction (Swift). Libraries were sequenced using an Illumina Nextseq500 sequencer. Quality and preprocessing of Swift libraries was done using Trim Galore. Genome alignment and base pair conversion was performed using Bismark.[47] Aligned bam files were then converted to '.mr' files using 'to-mr' from the Walt pipeline.[48] Duplicates were removed and methylation counts were calculated using 'methcounts'. Symmetric CpGs were extracted using 'symmetric-cpgs.' Hypomethylated regions were identified using the 'hmr' function from Walt.

Differential methylation analysis

Hypomethylated regions were first overlapped between conditions then the average methylation ratio was calculated across the shared region. Differentially hypomethylated regions were defined as regions that decreased in methylation by greater than 25% whereas hypermethylated regions gained more than 25% methylation. Only CpGs with greater than 5X coverage were considered. Differences in methylation ratios were statistically calculated using Fisher's exact test.

Methylation plotting

Methylation plots were generated in Python and R using the average methylation values calculated over a region of interest. MethRatio tables were compressed using tabix then averaged over either fixed width or variable length bins. Only CpGs with higher than 5X coverage were used. WGBS tracks were visualized using the Integrative Genomics Viewer.

QUANTIFICATION AND STATISTICAL ANALYSIS

Statistical analysis

Statistical testing for *in vivo* and *in vitro* biological assays was performed using GraphPad PRISM (v8.4.2). The numbers of replicates or samples is indicated in each figure legend as denoted by "n." Error bars indicate mean ± SEM (standard error mean) where indicated in Figure Legends. Tests across multiple groups were conducted using one- or two-way ANOVA unless otherwise indicated. Multiple hypothesis testing and p-value correction were used as indicated in the Figure Legends. Data were considered statistically significant at $*p < 0.05$, $**p < 0.01$, $***p < 0.001$.

Single cell RNA filtering and normalization

Further filtering and normalization of the 'cellranger aggr' output matrix was performed using Seurat (version 4.0.4). First, cells with greater than 10% mitochondrial reads, fewer than 500 genes per cell, and fewer than 100 mRNA molecules were removed. Libraries were then normalized using Seurat SCTransform and integrated using 'FindIntegrationAnchors' and 'IntegrateData.'

Mapping to Reference LSK scRNA dataset

As a reference dataset, we integrated 10X libraries from LSK cells derived from four 2-month-old mice. Reference libraries were sequenced using Illumina NovaSeq and normalized using Seurat SCTransform as described above. Reference cells were mapped to an average read depth of 150,000 reads per cell for 55,514 total cells. Clustering was performed using Seurat 'FindNeighbors' (dims = 1:10) and 'FindClusters' (resolution = 0.8). Query mapping was performed using Seurat 'FindTransferAnchors' (reference reduction = 'pca,' k.filter = NA) to assign predicted cell clusters and dimensional reduction based on PCA.

Integrated dataset clustering and annotation

To reduce noise and enable tuning of cluster assignment, we applied methods derived from Bioconductor Orchestrating Single Cell Analysis (https://github.com/OSCA-source/OSCA) to iterate clustering and achieve stable, pure clusters. Following reference cluster mapping, the integrated dataset was filtered for doublets using scDblFinder. Principal components were selected using 'getClusteredPCs' (scran package). Clustering was performed using 'buildSNNGraph' (k = 8, dimred = 'PCA') and clusters were assigned using 'cluster_walktrap.' To compute cluster modularity and purity, 'pairwiseModularity', 'approxSilhouette', and 'neighborPurity' (bluster R package) were applied. An adjusted Rand index for each cluster was calculated using 'bootstrapStability' (mode = 'index') and clustering was reiterated to remove small clusters and merge highly similar clusters using 'mergeCommunities.'

Cell type annotation was based on manual curation of marker genes and assignment using SingleR based on the Immgen database. Cell types were labeled as follows: LTHSCs: Slamf1^{Hi} Cd34^{Lo} Cd48^{Lo}); lympho-myeloid multipotent progenitors (LMPP: Slamf1^{Lo}Cd34^{Mid}); myeloid progenitors (MyMPP: Slamf1^{Lo}Cd34^{Mid}Flt3^{lo}Mpo^{Hi}Cebpa); common lymphoid progenitors (CLP: Cd34^{Mid}Flt3^{Hi}Gata2+); mast cell progenitors (Mast: Cd34^{lo}Apoe+Rap1a+); and megakaryocyte-erythroid progenitors (MEP: Slamf1^{lo}Cd34^{lo}Ebf1+).

Pseudotime lineage selection and assignment

To refine differentiation lineages and account for heterogeneity within different clusters, we applied parallel lineage inference and pseudotime techniques. Using TSCAN, we computed an unsupervised minimum spanning tree (MST) on our clustered dataset to generate cell cluster ordering. We then applied Slingshot, setting the most stem cell-like cluster (Cluster 6) as the root, and compared cluster ordering between TSCAN and Slingshot. Both methods showed high convergence of cluster orders when using unsupervised or partially supervised root-setting. We next annotated each predicted lineage trajectory using known markers of myeloid, lymphoid, or cell-specific differentiation markers. The LSK cell population contains a multitude of cell trajectories that, while highly studied, maintain highly debated cellular definitions. We therefore curated a set of marker genes to delineate trajectories at a global resolution, omitting complex bifurcations and cross-lineage identity transformations (markers genes listed above). Following TSCAN and Slingshot reordering, cells were assigned to their best-fit lineage trajectory.

scRNA differential gene expression and pathway enrichment

Within clusters, differential gene expression was performed using Seurat 'FindMarkers' (logfc.threshold = 0, min.pct = 0.3, test.use = 'MAST'). Between lineages, we applied the tradeSeq R package to identify genes that varied within lineages but between samples. Pathway enrichment was performed using 'fgseaMultilevel' (eps = 0) and 'msigdbr' to access MSigDB pathways.

Differential methylation analysis

Hypomethylated regions were first overlapped between conditions then the average methylation ratio was calculated across the shared region. Differentially hypomethylated regions were defined as regions that decreased in methylation by greater than 25% whereas hypermethylated regions gained more than 25% methylation. Only CpGs with greater than 5X coverage were considered. Differences in methylation ratios were statistically calculated using Fisher's exact test.